Systematics of pure and doped ^{4}He clusters

S. A. Chin
Center for Theoretical Physics and Department of Physics, Texas A&M University, College Station, Texas 77843

E. Krotscheck
Center for Theoretical Physics and Department of Physics, Texas A&M University, College Station, Texas 77843 and Institute for Theoretical Physics, University of California, Santa Barbara, California 93106

(Received 17 May 1994; revised manuscript received 2 May 1995)

Optimized variational calculations have been carried out for pure and doped clusters of ^{4}He atoms up to a cluster size of N=1000 particles. For small cluster sizes with less than or equal to 112 particles, where comparisons with existing diffusion Monte Carlo results are possible, we find excellent agreement for the ground-state energy, correlation, and structure functions. For larger clusters, our ground-state energies extrapolate smoothly toward a bulk limit of -7.2 K with a surface energy of 0.272 K Å^{-2}. The resulting ground-state densities show unmistakable oscillations, confirming our earlier conclusions based on diffusion Monte Carlo studies. The present study of large clusters allows us to bridge the gap between finite systems and the bulk limit. Specifically, we show how the bulk limit of collective energies is reached as well as how the bulk Feynman spectrum is reproduced in the S-wave component of the dynamic structure function in large droplets. By plotting the collective excitation energy of higher multipole modes as a function of an effective wave number $k = \sqrt{\ell(\ell+1)}/R$, we show that the resulting spectrum can be directly compared with experimental excitation energies determined for plane liquid surfaces and films. By summing up to $\ell = 50$ partial wave components, we show that the full dynamic structure function simultaneously displays the phonon-roton and the ripplon excitation spectrum. In the case of helium droplets doped with impurities such as rare gas atoms or the SF_6 molecule, we show that the dipole collective mode becomes unstable with increased droplet size, strongly indicating that these impurities are delocalized inside large droplets. The microscopic character of the instability is revealed in the excitation functions and transition densities of the dipole mode. The introduction of impurities also profoundly alters the dynamic structure function, severely "fragments" the Feynman spectrum, and obliterates landmark structures such as the maxon and the roton.

I. INTRODUCTION

A current theme in the study of quantum liquids, both experimentally[1–9] and theoretically,[10–18] is to understand how various bulk physical properties are modified in restricted geometries. A converse theme is to understand how these various bulk properties actually emerge from finite systems. Helium clusters are unique in that they are the only known *bosonic*, fully quantum, finite bound state systems that can span the range from a few-particle bound state to that of the bulk limit. They are therefore an excellent laboratory for studying the finite-size dependence of physical properties. Moreover, because of the relative simplicity of the helium-helium interaction, helium clusters can be accurately solved by Monte Carlo methods or by sophisticated variational theory (as we will demonstrate below) without recourse to phenomenology or *ad hoc* modeling. One is therefore in an excellent position to concentrate on the physics involved rather than be distracted by discussions of approximate methods or modeling adequacy. The recent suggestion that the Bose condensate in droplets may be detectable via helium atom-cluster collision[18–20] has given further impetus to the study of helium clusters.

Recent calculations of the ground-state structure of quantum liquid droplets have been based on variational and diffusion Monte Carlo algorithms[15–17,21,22] and on density functional theory.[14,23–25] In this work, we take a different approach and apply the hypernetted-chain/Euler-Lagrange theory (HNC/EL) to the study of large helium clusters presently too time consuming for exact diffusion Monte Carlo (DMC) simulations. This theory has been shown to provide, for all cases studied so far, ^{4}He in three[26] and two[27,28] dimensions, ^{3}He-^{4}He-mixtures, atomic impurities[29] in ^{4}He, hard-sphere bosons, and the Fermi systems ^{3}He and $D_\uparrow$,[30] a predictive power within a few percent of diffusion or Green's function Monte Carlo (GFMC) calculations, but computationally about two or three orders of magnitude more efficient. The method avoids several difficulties that are encountered in stochastic methods when quantities other than the ground-state energy are of interest. For example, in the calculations of excited states in Ref. 21, it was necessary to calculate the partial wave expansion of the two-body density by a two-dimensional binning of approximately 4000 numbers. Reasonable statistics on these 4000 numbers then required rather long running time. Aside from statistical uncertainly, diffusion and Green's function Monte Carlo calculations in prac-

tice suffer from extrapolation errors when computing observables other than the energy, such as the two-body density. This error is particularly acute when the trial function, though providing a reasonable estimate of the energy, may nevertheless poorly model the exact wave function in details. In contrast, the optimized variational theory presented here is free from statistical or extrapolation uncertainties which are crucial for deciding fine structures such as the controversial density oscillations in helium clusters. Finally, the theory is manifestly microscopic in that it assumes no *a priori* information other than the Hamiltonian.

In comparison with our optimized (and unrestricted) variational theory, *variational Monte Carlo* (VMC) calculations require a certain amount of physical intuition to construct a sufficiently accurate variational wave function. Minimizing the total energy of the system with respect to a few parameters gives *some,* but not necessarily *enough* guidance for the construction of an accurate variational wave function. In particular, in the present case, the ground-state energy is, in the vicinity of the bulk saturation density, a very slowly varying function of the density which makes finding its true minimum very difficult. Moreover, since the error in the ground-state energy is only of second order in terms of the error in the trial wave function, the ground-state energy is rather insensitive to fine details of the wave function. As a consequence, results other than the energy computed in this manner may be strongly biased by the user's physical intuition or prejudice. The problem is of immediate relevance for the quadrupole excitation in large droplets, which is a surface excitation. In cases where the variational wave function is not sufficiently flexible, energy minimization may well tune the wave function for a good description of the bulk interior, but still leave the surface area poorly described. The same problem also appeared in our DMC calculations, where a variational wave function is used as a reference for extrapolation. As a consequence, our extrapolation corrections were largest for the quadrupole excitation.

On the other hand, *density functional* calculations[23,14,31,24,25] are computationally quite straightforward. By construction, these theories rely on phenomenological inputs from systems *other* than the one under examination, and occasionally, as in the local density approximation, on systems that do not exist and cannot be produced in nature (uniform low density liquid helium). The validity of such an extrapolation into unphysical regimes must always be scrutinized. In particular, when two-dimensional substructures like layers or shells are part of the system under consideration, presently available phenomenological density functionals[23,31] have been proven to be unreliable.[28]

By use of our optimized variational theory, we have computed the ground-state energy, chemical potential, collective monopole, dipole, quadrupole, and higher multipole excitations, one and two-body densities, and the dynamic structure function for pure and doped (rare gas atoms and SF_6) helium clusters up to size $N = 1000$. This allows us to address specific questions left unresolved by our DMC calculations:

(a) The diffusion Monte Carlo calculations of Ref. 21 have been carried out to a very high precision because two-body densities with good statistics are essential for applying the generalized Feynman theory of excitations. These calculations have revealed, similar to the GFMC calculations of Helmbrecht and Zabolitzky,[10] an oscillating one-body density traceable to the "shell structure" of the ground state. However, because of the intrinsic statistical limitation of stochastic methods, this structure is still under dispute. Since questions of convergence and extrapolation errors for such a fine structure can be fairly difficult or time consuming to address, it is useful to have this issue resolved by an entirely different approach with proven reliability. Our optimized variational results, which are unbiased by any phenomenological input, leave no doubt that density oscillations exist in helium clusters.

(b) Since precision in computing the two-body density requires lengthy simulations, the Monte Carlo calculation of droplet excitations, even on a supercomputer, is limited to rather small cluster sizes. This has prevented us from seeing the actual emergence of bulk properties from finite systems. In the HNC/EL method, the two-body density is directly computed and the size of the clusters under consideration is limited only by the available computer memory for its storage. In this work, we have no problem evaluating cluster properties with sizes on the order of 1000 particles on a fast workstation. One of the striking findings of this work is the emergence of both a narrow phonon/roton spectrum *and* a ripplon spectrum in large clusters with $N \geq 240$. Moreover, by systematically studying the ground-state and excitation energies as functions of cluster size, one can reliably estimate the regime of validity of the liquid drop model. In future applications, it would also be possible to use correlated basis functions (CBF) theory for calculating corrections to the low-lying excitation spectrum in a manner similar to our excitation calculations for helium films.[32–34]

(c) In our previous DMC calculation, the computation of low-lying collective excitations requires the input of the partial wave amplitudes of the two-body density. Since in Monte Carlo calculations, higher-ℓ partial wave amplitudes have lower signal-to-noise ratio, only the $\ell = 0, 2$ collective modes were studied. In this work, we can easily compute collective excitations up to $\ell = 50$ and can therefore study in detail the high-ℓ, surface excitation of the helium droplet as well as the full, partial-wave summed, dynamic structure function.

(d) The introduction of impurity atoms and molecules into helium clusters profoundly alters its excitation properties. In this case, the dynamics structure function reveals that the Feynman spectrum is fragmented to such an extent that it is without recognizable features such as the maxon and the roton. Furthermore, our systematic study of the excitations reveals an instability of the *dipole excitation*, suggesting that the spherically symmetric droplet configuration is unstable against infinitesimal translation of its center with respect to impurities such as rare gas atoms or SF_6 molecules. Such an instability may signal the onset of spontaneous deformations of the droplet, leading to the possibility of delocalization of the impurity. Such a delocalization scenario

has been proposed in recent experimental findings,[7,8] but has also been challenged.[9] Current Monte Carlo calculations[22,35,36] on this question remain controversial and inconclusive.

Finally, as a new formal development, which will also be relevant for the application of variational methods to nuclear and other finite systems, we show how the center-of-mass motion can be treated in an optimized variational calculation. The Jastrow-Feenberg ground state (2.2) is translationally invariant only for very simple pair (and triplet) correlations that depend only on the pair separations of particles. However, the comparison between DMC and VMC calculations raises doubt that such simple correlation functions describe the full physics.

The paper is organized as follows: Sec. II presents our results on the structure and the low-lying collective excitations of pure droplets. Section III carries out a similar analysis for clusters doped with rare gas atoms or a SF_6 molecule. In Sec. IV we will carry out a systematic analysis of low-lying, high angular momentum excitations, and Sec. V shows results on the dynamic structure function for both pure and doped droplets. A series of appendixes gives details of our treatment of the center-of-mass motion, discusses some properties of the Euler equations which are important for a careful calculation of excitation energies in finite systems, and describes our treatment of triplet correlations.

II. GROUND AND EXCITED STATES OF PURE ^{4}He CLUSTERS

Our optimized variational theory begins with the Hamiltonian,

$$H = -\frac{\hbar^2}{2m}\sum_i \nabla_i^2 + \sum_{i<j} v(|\mathbf{r}_i - \mathbf{r}_j|), \tag{2.1}$$

where one normally uses the Aziz[37] potential for the two-body interaction. The method is *approximate* since it is based on a variational wave function of the Jastrow-Feenberg type,

$$\Psi_0(\mathbf{r}_1,\ldots,\mathbf{r}_N) = \exp\frac{1}{2}\left[\sum_i u_1(\mathbf{r}_i) + \sum_{i<j} u_2(\mathbf{r}_i,\mathbf{r}_j) + \sum_{i<j<k} u_3(\mathbf{r}_i,\mathbf{r}_j,\mathbf{r}_k)\right], \tag{2.2}$$

and uses integral equation techniques to calculate the physical quantities of interest. The one-body function $u_1(\mathbf{r})$ impresses the nonuniform structure, the two-body function $u_2(\mathbf{r}_i,\mathbf{r}_j)$ deals with the short-ranged repulsion, and the three-body function $u_3(\mathbf{r}_i,\mathbf{r}_j,\mathbf{r}_k)$ describes triplet correlations. The correlations are assumed to be the most general ones permitted by the geometry; for example, the pair-correlation function $u_2(\mathbf{r}_i,\mathbf{r}_j)$ depends on the distance between these two particles, *and* on the distance of both particles from the center of the droplet. These correlations are determined by solving the Euler equations

$$\frac{\delta E_0}{\delta u_n(\mathbf{r}_1,\ldots,\mathbf{r}_n)} = 0, \qquad n = 1,2,3 \tag{2.3}$$

in an unrestricted function space [a slight modification of Eq. (2.3) for a finite system will be discussed below]. The energy expectation value E_0 and a numerically tractable formulation of the Euler equations (2.3) can be calculated using the hierarchy of hypernetted chain (HNC) approximations. A rather simple, universal estimate of higher-order "elementary" diagrams has proven to provide excellent results[26] for all cases where experimental data or exact calculations are available for comparison.

Besides the ground-state energy, quantities of interest are the one- and two-body densities

$$\rho_1(\mathbf{r}) = \frac{\langle\Psi_0 \mid \sum_i \delta(\mathbf{r}_i - \mathbf{r}) \mid \Psi_0\rangle}{\langle\Psi_0 \mid \Psi_0\rangle}, \tag{2.4}$$

$$\rho_2(\mathbf{r},\mathbf{r}') = \frac{\langle\Psi_0|\sum_{i\neq j}\delta(\mathbf{r}_i - \mathbf{r})\delta(\mathbf{r}_j - \mathbf{r}')|\Psi_0\rangle}{\langle\Psi_0 \mid \Psi_0\rangle}, \tag{2.5}$$

and the coordinate-space representation of the static structure function

$$S(\mathbf{r},\mathbf{r}') = \delta(\mathbf{r}-\mathbf{r}') + \frac{\rho_2(\mathbf{r},\mathbf{r}') - \rho_1(\mathbf{r})\rho_1(\mathbf{r}')}{\sqrt{\rho_1(\mathbf{r})\rho_1(\mathbf{r}')}}. \tag{2.6}$$

The one- and two-body densities are necessary inputs to the calculation of excitation energies and the dynamic structure function.

The general theory of optimized correlation functions has been discussed in sufficient detail in Refs. 38, 39, and 27. In this work, we have implemented the theory including elementary diagrams and optimized triplet correlations as described in Ref. 27. The basic difference between the present calculations and those presented in Ref. 27 is that we work in a spherical instead of a plane-surface geometry. In the previous case, all two-body quantities are functions of the distances z and z' of each of the particles from the surface, and their distance $r_\parallel$ in the direction parallel to the surface; the Euler equations can be decoupled in the momentum parallel to the surface. In the droplet case, all two-body quantities are functions of the distances r and r' of each of the particles from the center, and the angle θ between the coordinate vectors. In this case, the Euler equations can be decoupled in spherical partial waves. For the purpose of this work, it is sufficient to concentrate on the only new technical aspect of the theory, which is concerned with the treatment of the center-of-mass motion. This modification of the theory is essential since the most general Jastrow-Feenberg wave function (2.2) is not translationally invariant.

For finite systems we must consider the "internal energy" rather than the total energy,

$$E_{\rm int} = E - T_{\rm cm}. \tag{2.7}$$

$T_{\rm cm}$ is the expectation value of the kinetic energy connected with the center-of-mass motion

$$T_{\rm cm} = \frac{\langle\Psi_0 \mid \hat{T}_{\rm cm} \mid \Psi_0\rangle}{\langle\Psi_0 \mid \Psi_0\rangle}, \qquad \hat{T}_{\rm cm} \equiv -\frac{\hbar^2}{2M}\left|\sum_i \nabla_i\right|^2, \tag{2.8}$$

where $M = Nm$ is the total mass of the droplet.

At first glance, the issue appears to be academic since we are mostly dealing with *large* droplets, and the center-of-mass motion should be negligible. Moreover, the inhomogeneous hypernetted chain equations are accurate only to order $1/N$; in other words, the expected accuracy of the theory is, at best (i.e., even if all diagrams were calculated exactly), of the order of $1/N$. The subtle point is that the inclusion of the center-of-mass energy is essential for computing the excited states. Since the calculation of the excitation spectrum is an integral part of the numerical optimization of the correlations, some care must be exercised to avoid spurious solutions or instabilities. Of course, the expected smallness of center-of-mass effects will allow us to make significant simplifications. The modifications of the theory and the resulting Euler equations resulting from the inclusion of the center-of-mass motion will be described in Appendix A.

A. Ground-state properties

The Euler equation resulting from the extremum condition (2.3) can be formulated in terms of the local particle-hole interaction

$$V_{\text{p-h}}(\mathbf{r}_1, \mathbf{r}_2) \equiv \frac{\delta^2 E}{\delta\rho(\mathbf{r}_1)\delta\rho(\mathbf{r}_2)} \tag{2.9}$$

and is conveniently solved in the normal-mode representation (A18). Using the normal-mode representation (A21) it is easy to demonstrate that the eigenvalues of this equation are also the eigenvalues of the generalized Feynman equation (A23). Furthermore, the normal-mode decomposition is just the representation of the static structure function as an energy integral of the dynamic structure function.[21] The particle-hole interaction is obtained iteratively, starting from an initial guess, by solving Eqs. (A14), (A15), and (A17). Once convergence is achieved, physical quantities such as the one- and two-body densities, Feynman spectrum, static and dynamic structure function, etc., are simultaneously determined. This is the essential difference from our previous DMC based calculation, where the two-body density (2.5) and the coordinate-space representation (2.6) of the static structure function are the principal ingredients of input upon which the generalized Feynman equation (A23) for the excited states is solved.

Table I shows a comparison of our HNC/EL results with some other calculations, mostly different versions of our DMC simulations of Ref. 21. For completeness and comparison, we show in the last row of Table I the results of the nonlocal density approximation (NLDA) calculation by Casas and Stringari,[14] based on a nonlocal density functional (NLDF), and those of a finite-range density-functional calculation (FRDF) of Ref. 25. The results of our HNC/EL calculations for both the ground-state energy and the unit radius $r_0 = (5/3)^{1/2}\langle r^2\rangle^{1/2}N^{-1/3}$ agree with our earlier DMC calculations better than expected. The best global fit to the energy per particle for clusters with 70 or more particles has been obtained by the form

$$\frac{E(N)}{N} = -7.21 + 17.71N^{-1/3} - 5.95N^{-2/3}\ \text{K}. \tag{2.10}$$

Clusters with 20 and 40 particles are basically surface dominated clusters whose central densities have not yet reached the bulk value. They were therefore deemed unsuitable for use in extrapolating the bulk limit. In Fig. 1 we show our HNC/EL results, together with the above fit and the DMC results of Ref. 21. Equation (2.10) suggests an asymptotic energy per particle of -7.21 K and a surface energy of $\sigma \approx 0.284\ \text{K Å}^{-2}$. The asymptotic energy has the expected accuracy due to our treatment of elementary diagrams, demonstrating that any simplifications of the numerical treatment imposed by the nonuniform geometry have no detrimental effect on the bulk energy. The surface energy also compares quite favorably with the experimental value[40] of $0.256\ \text{K Å}^{-2}$. The value of $0.284\ \text{K Å}^{-2}$ is improved to $\sigma_{\text{HNC}} \approx 0.272\ \text{K Å}^{-2}$ when the slightly lower calculated central density ($0.02\ \text{Å}^{-3}$) is used instead of the experimental value of $0.02185\ \text{Å}^{-3}$.

TABLE I. Ground-state properties of ^{4}He clusters as computed by various methods. $\epsilon_0 = E_0/N$ is the ground-state energy per particle in degrees K, $r_0 = (5/3)^{1/2}\langle r^2\rangle^{1/2}N^{-1/3}$ is the unit radius defined from $\mathbf{r}_{\text{cm}}$ in units of Å. VMC-II and DMC-II refer to our variational and diffusion Monte Carlo calculations of Ref. 21, NLDA to the nonlocal density approximation of Ref. 14, and FRDF to the finite-range density-functional theory of Ref. 25.

	HNC/EL		VMC-II		DMC-II		NLDA		FRDF	
	ϵ_0	r_0	ϵ_0	r_0	ϵ_0	r_0	ϵ_0	r_0	ϵ_0	r_0
20	-1.677	2.83	-1.522(2)	2.68	-1.659(3)	2.68	-1.27	3.11	-1.40	2.87
40	-2.570	2.59	-2.344(1)	2.53	-2.538(4)	2.53	-2.18	2.74	-2.27	2.60
70	-3.273	2.47	-2.966(1)	2.46	-3.205(4)	2.43	-2.93	2.57	-2.97	2.48
112	-3.801	2.40	-3.427(2)	2.40	-3.726(4)	2.42	-3.51	2.47	-4.28	2.41
150	-4.095	2.37								
200	-4.362	2.35								
240	-4.521	2.35							-4.28	2.33
400	-4.928	2.33								
600	-5.211	2.33								
800	-5.377	2.33								
1000	-5.503	2.33								

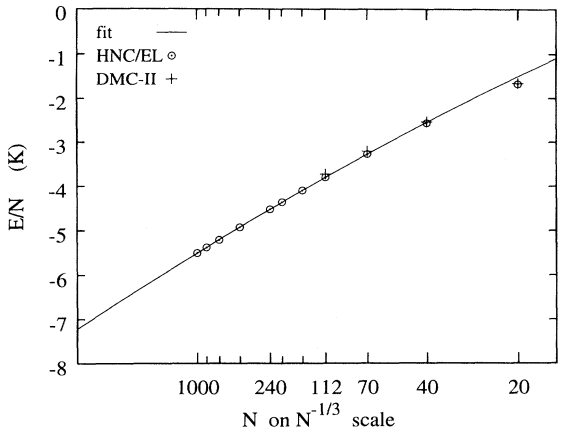

FIG. 1. The HNC/EL energies of helium clusters (circles) are compared with the DMC results of Ref. 21 (crosses). Also shown is the fit (2.10) (solid line); recall that only the energies for particle numbers $N \geq 70$ have been fitted.

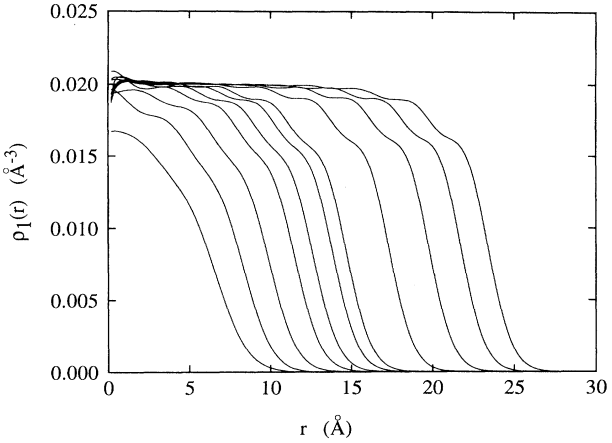

FIG. 3. The ground-state density profiles of ^{4}He droplets with particle numbers $N = 20, 40, 70, 112, 150, 200, 240, 400, 600, 800$, and 1000 as obtained from the HNC/EL theory.

For the density profiles (cf. Fig. 2), the agreement between our HNC/EL calculations and the DMC results is less quantitative. They are systematically too low in comparison and appear to converge towards a central density slightly larger than 0.02 Å^{-2} (cf. Fig. 3). Such a small deviation is easily understood from the fact that the ground-state energy of bulk ^{4}He is, in the vicinity of the saturation density, a very weakly varying function of the density. If the fitted bulk liquid equation of state by de Bruyn Ouboter and Yang[41] is extrapolated to $\rho = 0.02$ Å^{-3}, the ground-state energy only increases by a mere 0.07 K per particle. We do not claim that

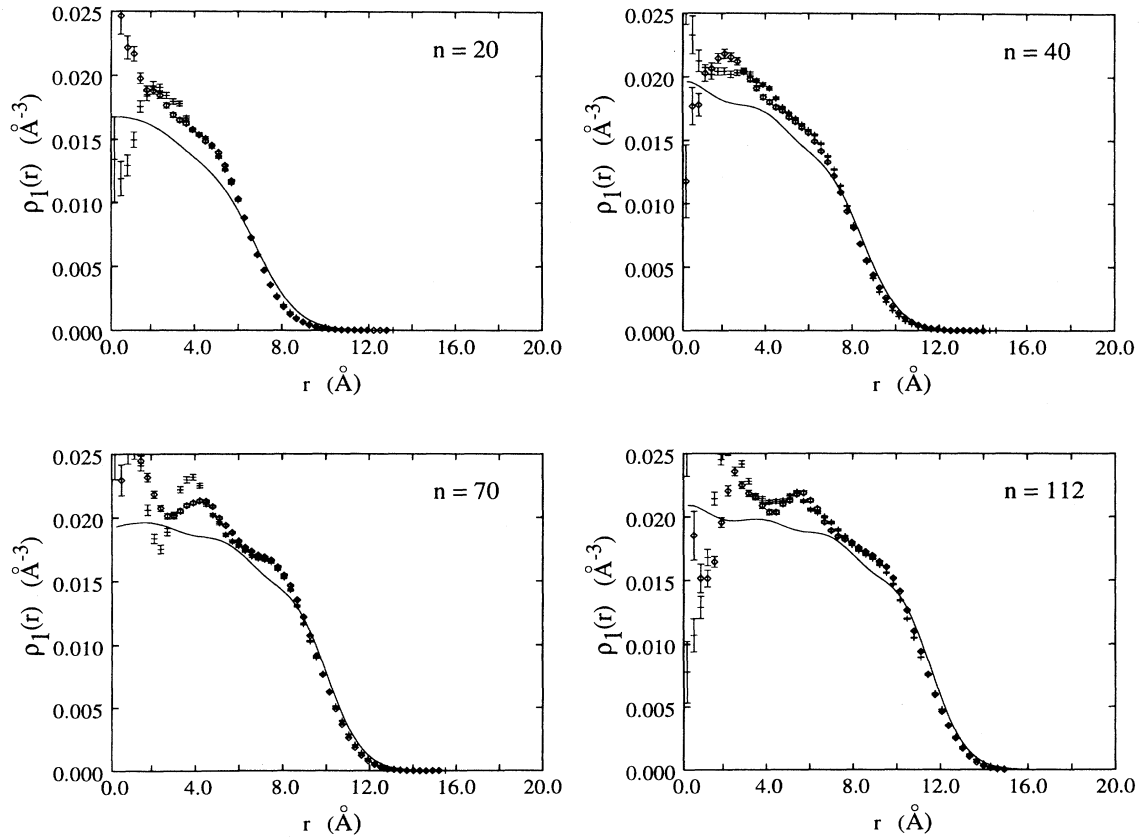

FIG. 2. The ground-state density profiles of ^{4}He droplets from the HNC/EL theory (solid lines) are compared with the DMC results of Ref. 21 (asterisks and diamonds with error bars).

HNC/EL is sensitive to this level of accuracy. While it would have been easy to produce a better match between ours and the DMC densities by judiciously choosing our treatment of elementary diagrams, we have decided not to do so and are using the theory exactly the same way as in our calculations of bulk quantum liquids[26] and quantum liquid films.[27] We suspect that the slight mismatch between the equilibrium density of the bulk liquid and the central cluster density is due to some numerical sacrifices that were made in the calculation of the so-called elementary diagrams, which were calculated in a spherically averaged approximation.

In our previous DMC calculation in Ref. 21, we have found persistent ground-state density oscillations in smaller clusters attributable to geometric "shell structures." Our present calculations clearly demonstrate that the one-body densities are indeed *not* smooth. Moreover, Fig. 3 shows that the outermost shell structure in smaller clusters has developed into a broader shoulder in the density profile of larger clusters, suggesting a two-dimensional "skin" of ^{4}He surrounding each cluster. A similar shoulder in the profile has been found in our calculations of thick absorbed films.[32]

These density oscillations from our HNC calculations are somewhat smaller in amplitude and out of phase with those found in DMC, but they are undeniably present and are rather similar. For each N, they have about the same number of oscillations. The reduction in amplitude may be due to the lower density of our HNC/EL clusters. This is supported by the fact that when we ignore the elementary diagrams and triplet correlations, the theory reproduces the well-established lower saturation density of the HNC *approximation* of $\rho_0^{\rm HNC} \approx 0.017$ Å^{-3}, and the density oscillations disappear altogether. The fact that these density oscillations are dictated by elementary diagrams and triplet correlations may well explain why they cannot be seen in VMC calculations with simple trial functions. These oscillations are most prominent near the surface and are less conspicuous as one moves toward the center. (The large density fluctuations near $\mathbf{r} = 0$ in DMC droplets are artifacts of binning and should be discounted.) Similar density oscillations have also been seen recently in an improved density functional calculation of Dalfovo, Lastri, and Stringari.[42]

A comparison of the energetics and the global structure of the physical system, such as the one-body density, is normally insufficient to document the efficiency and accuracy of a given theory for describing the physical system. Other quantities that must be considered are the pair density, pair distribution functions, and the static structure function. For all of these quantities, Monte Carlo results exist for small clusters and experimental data are available in the infinite bulk limit. By comparing these with our theoretical findings, one can judge both the quality of our theory, and, once that is established, the systematics of its predictions in approaching the bulk limit.

The pair-distance distribution $\rho_2(r)$ is defined by

$$\rho_2(r) = \int d^3r_1\, d^3r_2 \delta(r - |\mathbf{r}_1 - \mathbf{r}_2|)\rho_2(\mathbf{r}_1, \mathbf{r}_2). \tag{2.11}$$

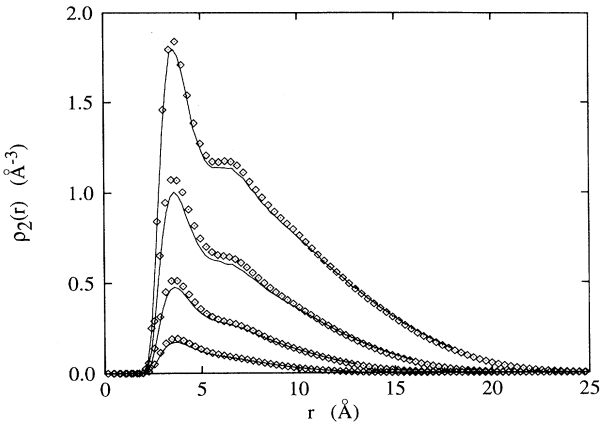

FIG. 4. The pair-distance distribution function as defined by Eq. (2.11) for cluster sizes (from bottom to top) N =20, 40, 70, and 112 particles. The diamonds are DMC-II results from Ref. 21, and the solid lines are results of the present work.

Figure 4 shows a comparison between our HNC/EL result with those of DMC in Ref. 21. Note that even small details, such as the height of the second-neighbor peak, are well reproduced. The first peak height is slightly below that of DMC, which again may be attributed to our lower central droplet density.

In order to study how the bulk limit is approached in larger clusters, the normalization of the pair-distance distribution function (2.11) must be modified to extract the usual pair-correlation function. In the bulk limit, the two-body density has the form $\rho_2(\mathbf{r}_1, \mathbf{r}_2) = \rho^2 g_2(|\mathbf{r}_1 - \mathbf{r}_2|)$, and hence $\rho_2(r) = N\rho g_2(r)$, where ρ is the bulk density. We therefore define

$$g_2(r) \equiv \frac{1}{N\rho}\rho_2(r), \tag{2.12}$$

which has the virtue of being simply proportional to the pair-distance distribution. The resulting $g_2(r)$ is shown in Fig. 5. It certainly has the qualitative feature expected of a pair-correlation function. However, its approach toward the bulk limit is rather slow. To illustrate the fact that the convergence to the bulk limit can depend strongly on one's definition of the corresponding quantity in the *finite* system, we start from the *two-body correlation function* $g_2(\mathbf{r}_1, \mathbf{r}_2)$ defined by

$$\rho_2(\mathbf{r}_1, \mathbf{r}_2) \equiv \rho_1(\mathbf{r}_1)\rho_1(\mathbf{r}_2)g_2(\mathbf{r}_1, \mathbf{r}_2). \tag{2.13}$$

In the bulk limit $N \to \infty$, $g(\mathbf{r}_1, \mathbf{r}_2) \to \bar{g}(|\mathbf{r}_1 - \mathbf{r}_2|)$, which is identical to the above $g(r)$. However, even when $N \neq \infty$, one can still extract an *averaged* pair-correlation function $\bar{g}_2(r)$ via

$$\bar{g}_2(r) \equiv \frac{1}{V}\int d^3r_1\, d^3r_2 \delta(r - |\mathbf{r}_1 - \mathbf{r}_2|)\frac{\rho_2(\mathbf{r}_1, \mathbf{r}_2)}{\rho_1(\mathbf{r}_1)\rho_1(\mathbf{r}_2)}, \tag{2.14}$$

which is in general different from $g_2(r)$. V is the normalization volume. The resulting $\bar{g}_2(r)$'s are shown in Fig.

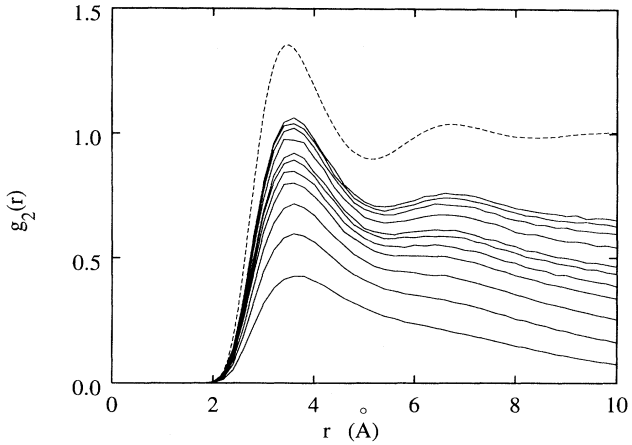

FIG. 5. The *normalized* pair-distance distribution function as defined in Eq. (2.12) is shown for cluster sizes (from bottom to top) N =20, 40, 70, ..., 1000 particles. The peak of the pair-density distribution function increases with increasing particle number. The dashed line is the pair distribution function of the bulk liquid calculated at the same density from Ref. 26.

6 and compared with the bulk limit at the same density. The convergence here is obviously much more rapid and in excellent agreement with the bulk result.

While the pair distribution functions $g_2(r)$ and $\bar{g}_2(r)$ reflect the short-range structure of the system crucial for a physical reliable description, it is the *static structure function* that is directly measured in scattering experiments. The static structure function can be obtained either by a frequency integration of the dynamic structure function, as described below, or by a Fourier transform of the pair-distance distribution (2.11),

$$S(k) = \frac{1}{N}\int d^3r d^3r' \sqrt{\rho_1(\mathbf{r})\rho_1(\mathbf{r}')}\, e^{i\mathbf{k}\cdot(\mathbf{r}-\mathbf{r}')} S(\mathbf{r},\mathbf{r}') = 1 + \frac{1}{N}\left\{\tilde{\rho}_2(k) - |\tilde{\rho}_1(k)|^2\right\}, \quad (2.15)$$

where $\tilde{\rho}_2(k)$ and $\tilde{\rho}_1(k)$ are Fourier transforms of the pair-distance and one-body densities, respectively.

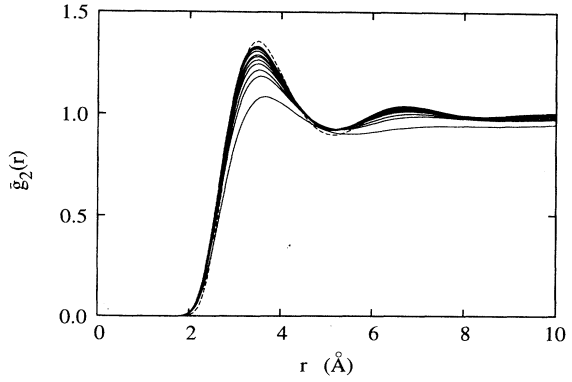

FIG. 6. Same as Fig. 5, but for the averaged pair distribution function (2.14).

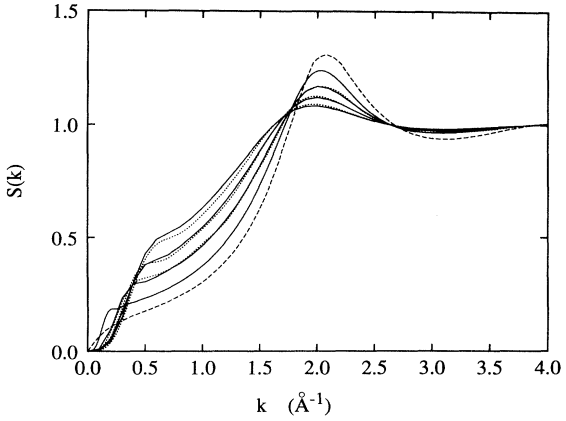

FIG. 7. The static structure function $S(k)$ [Eq. (2.15)] is shown for cluster sizes of 20, 40, 112, and 1000 particles (solid lines). The three dotted lines are the results of the DMC calculation of Ref. 21 for 20, 40, and 112 particles, and the dashed line is the bulk $S(k)$ at the calculated central density from Ref. 26.

In Fig. 7 a representative set of our HNC/EL static structure functions is compared with available DMC results[21] and with the bulk limit. Except for some slight differences (not too visible in the graph) near the "knee" region ($k \approx 0.3$) and for the particular case of $N = 20$, the overall agreement is again excellent. However, even for a very large droplet, the cluster $S(k)$ has yet to attain the full peak height of the bulk static structure function at the same density. Since $S(k)$ is related to $g_2(r)$, and specifically the peak in $S(k)$ to the the long-range oscillations of $g_2(r)$, this slow convergence is not unexpected. Another region of slow convergence is the existence of the "knee" at small k, which is clearly a finite-size effect that systematically diminishes with increased cluster size. For a finite system, one can easily show[43] that $S(k) \propto k^4$ in the limit of $k \to 0$. In the bulk limit, however, $S(k) \propto k$ as $k \to 0$. Thus $S(k)$ must change from the former to the latter as $N \to \infty$. This change is achieved by continuously shrinking the region where $S(k) \propto k^4$, whose border forms a characteristic "knee." This region extends roughly from $k = 0$ to $k = 2\pi/D$, where D is the diameter of the droplet. Since the latter goes as the cube root of N, the convergence is, not surprisingly, slow.

An alternative way to calculate the static structure function, which gives some more information on the physical processes contributing to it, is to start from the two-body density. The determination of the full two-body density $\rho_2(\mathbf{r},\mathbf{r}')$ is an integral part of our optimization procedure and will be discussed in the next section. Fundamental to our algorithm and the solution of the optimization problem is the partial-wave analysis of all quantities involved, for example,

$$\rho_2(\mathbf{r},\mathbf{r}') = \sum_\ell \frac{2\ell+1}{4\pi}\rho_2^{(\ell)}(r,r')P_\ell(\hat{\mathbf{r}}\cdot\hat{\mathbf{r}}'), \quad (2.16)$$

from which we obtain the partial-wave components of the

pair distribution function

$$g_2^{(\ell)}(r,r') = \frac{\rho_2^{(\ell)}(r,r')}{\rho_1(r)\rho_1(r')}, \tag{2.17}$$

and a partial-wave expansion of the static structure function

$$S(k) = \sum_\ell S_\ell(k), \tag{2.18}$$

$$S_\ell(k) = \delta_{\ell,0} + \frac{2\ell+1}{4\pi N}\int d^3r\, d^3r'\, \rho(r)\rho(r') j_\ell(kr) j_\ell(kr') \times \left[g_2^{(\ell)}(r,r') - 4\pi\delta_{\ell,0}\right]. \tag{2.19}$$

Both the multipole components of the pair distribution function, the individual components $S_\ell(k)$ of the static structure function, and the convergence of the series (2.18) are of interest. The first three multipole components of the pair distribution function for $N = 1000$ are shown in Fig. 8. The comparison with the equivalent figure of Ref. 21 shows that the HNC equations solve one of the most serious problems of the DMC calculation, namely, the contamination of the data by statistical fluctuations. Figure 9 shows the convergence of the series (2.18) for the same particle number. Specifically, we show the partial sum

$$S_L(k) = \sum_{l=0}^{L} S_\ell(k) \tag{2.20}$$

for $0 \le L \le 50$. It is clearly seen that it takes quite a few multipole components to reach convergence. This slow convergence of the multipole expansion of the static structure function will also be reflected further below when we study the dynamic structure function and its individual multipole components.

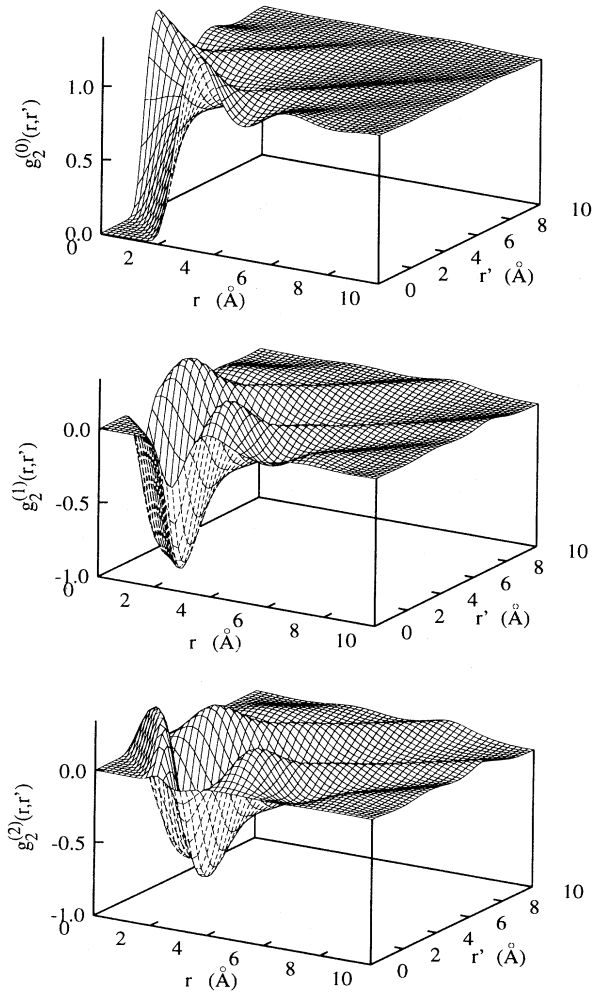

FIG. 8. The first three multipole components of the pair distribution function, $g_2^{(\ell)}(r,r')$, as defined in Eq. (2.17), are shown for $N = 1000$. Note that our definition deviates from the one used in Ref. 21 by a factor $2\ell + 1$.

B. Collective excitations

Excited states can be estimated by assuming a variational ansatz for the wave function of the excited state of Feynman form,

$$\Psi_F(\mathbf{r}_1,\ldots,\mathbf{r}_N) = F(\mathbf{r}_1,\ldots,\mathbf{r}_N)\Psi_0(\mathbf{r}_1,\ldots,\mathbf{r}_N) = \sum_{i=1}^{N} f(\mathbf{r}_i)\Psi_0(\mathbf{r}_1,\ldots,\mathbf{r}_N), \tag{2.21}$$

where the *excitation function* $f(\mathbf{r}_i)$ is determined by minimizing the excitation energy,

$$\hbar\omega \equiv E_F - E_0 = \frac{1}{2}\frac{\langle\Psi_0|[F,[T,F]]|\Psi_0\rangle}{\langle\Psi_0|F^2|\Psi_0\rangle}. \tag{2.22}$$

This minimization leads[44] to the generalized eigenvalue problem (A23). For each energy $\hbar\omega$, the corresponding excitation function $f(\mathbf{r})$ is related to an eigenfunction of the Euler equation (A18) through

$$\psi_\omega(\mathbf{r}) = \sqrt{\rho(\mathbf{r})} f(\mathbf{r}), \tag{2.23}$$

and the *transition density*, which is the time-dependent part of the density, through

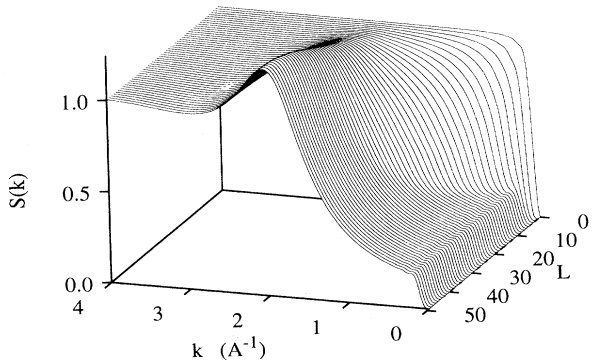

FIG. 9. The convergence of the series (2.20) of multipole components $S_\ell(k)$ to the structure function $S(k)$ is shown for the cluster sizes of $N = 1000$ for $L \le 50$.

$$\sqrt{\rho_1(\mathbf{r})}\phi_\omega(\mathbf{r}) = \delta\rho_\omega(\mathbf{r}), \tag{2.24}$$

to the adjoint states. As discussed in Appendix B, a *rigid* translation corresponds to an excitation function $f(\mathbf{r}) = \mathbf{c}\cdot\mathbf{r}$, whereas a constant excitation function corresponds to a renormalization of the wave function. For a variational ground-state wave function Ψ_0, Eq. (2.22) follows from the extremum condition (2.3). In our previous works on collective excitation based on DMC results, the generalized eigenvalue equation (A23) resulting from (2.22) was solved by a partial-wave expansion with inputs of one- and two-body densities.[21] In our current variational theory, the calculation of excitation energies and excitation functions is a part of the minimization procedure. The random-phase aproximation (RPA) equation (A18) solved in this procedure is, up to algebraic manipulations and the application of center-of-mass corrections, identical to the linear response equation used in Refs. 14 and 25.

Our results for monopole and quadrupole excitation energies are compared with our previous DMC energies and a few more recent calculations in Figs. 10 and 11. Overall, we find satisfactory agreement between our HNC/EL calculations and our Monte Carlo results. Both exhibit the same trend as a function of the cluster size. The fact that the present results are, for smaller particle numbers, somewhat below the Monte Carlo results is presumably due to the lower density of the systems—the droplets are "softer." At higher particle numbers, especially in the case of the quadrupole, Monte Carlo results

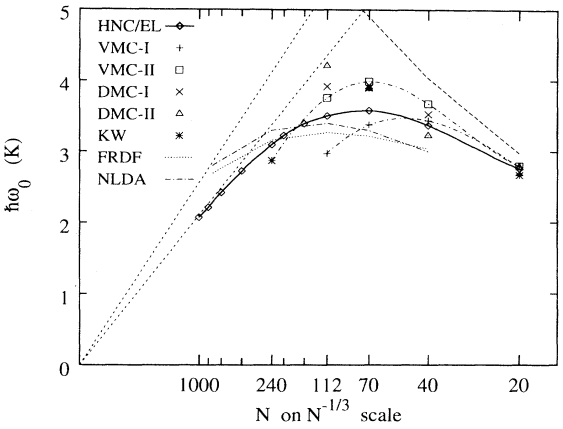

FIG. 10. The monopole excitation energies of droplets with up to 1000 particles (heavy solid line with diamonds) are compared with the results of our earlier DMC calculations (VMC-I, VMC-II, DMC-I, and DMC-II), those of Krishna and Whaley (Ref. 15), and two density functional calculations by Casas and Stringari (Ref. 14) and Barranco and Hernandez (Ref. 25). The long-dashed line is the continuum limit $-\mu(N)$. The upper short-dashed line is the liquid drop prediction as calculated from the *bulk* equation of state, and the lower dashed line is what appears to be an "extrapolated" liquid drop limit from the microscopic calculation of the excitation energies. Our VMC-II results have been extrapolated to the result of Krishna and Whaley through the dash-dotted line.

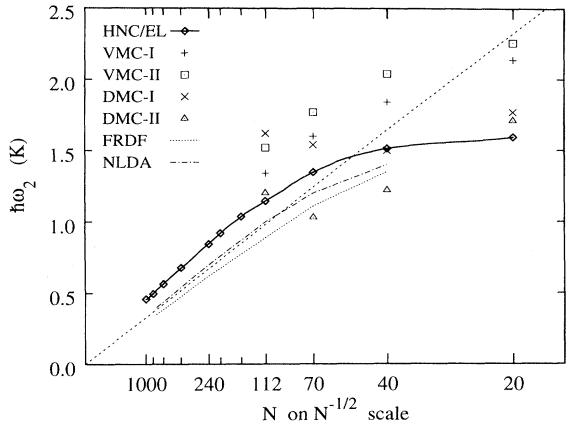

FIG. 11. Same as Fig. 10 for the quadrupole excitation energies. No extrapolation towards a "liquid drop limit" has been attempted in this case.

are less reliable due to extrapolation uncertainties in the one- and two-body densities.

We have also attempted an extrapolation to a liquid drop model limit. In the case of the monopole, the excitation energy appears to have approached such a limit quite well, albeit with a different slope. From the bulk equation of state, one would expect an asymptotic form for the monopole energy in the limit of large particle numbers,

$$\hbar\omega_0 = \frac{\hbar c\pi}{R} = 25.6N^{-1/3}\ \mathrm{K}, \tag{2.25}$$

whereas Fig. 10 suggests a coefficient of 21. This number is actually in quite good agreement with the prediction from the *calculated* equation of state,[26] which yields, at the *calculated* central density, a coefficient of 20. Some mismatch between the compressibility obtained from the equation of state and from the low-lying excitations is to be expected: It is quite well known that, within a microscopic theory, the compressibility obtained from the equation of state agrees with the compressibility obtained from the long-wavelength excitations only if *all* (Feynman or Jastrow-Feenberg) diagrams are calculated. Thus, the mismatch between the liquid drop limit as calculated from the excitations and as calculated from the bulk equation of state may be used as a quantitative measure of the quality of our variational calculation.

We note, however, that the convergence to a liquid drop limit in agreement with a bulk calculation is a mere consistency test of the calculation and not a prediction of the theory for the behavior of a finite system. A true *prediction* is how rapidly the liquid drop limit is approached as a function of the particle number. In that respect, both Monte Carlo and the present calculation indicate a significantly slower convergence towards the liquid drop limit than density functional calculations. This is consistent with our finding of Ref. 28 on liquid films.

In the case of the quadrupole excitations, the DMC calculations suffered from significant extrapolation un-

certainties as alluded to earlier. It is again important to know to what extent a "liquid drop limit" has been reached for cluster sizes considered here. Figure 11 seems to indicate that one is still far from such a limit. However, one can extract further information on "how close" one is to the liquid drop limit by considering higher multipole excitation modes. We will consider these primarily surface excitations in Sec. IV. As we shall see, for somewhat shorter wavelengths, the agreement between the dispersion relation of the surface modes calculated from the Feynman theory and the one calculated from the surface energy extracted from the mass formula (2.10) is indeed excellent.

III. GROUND AND EXCITED STATES OF DOPED ^{4}He CLUSTERS

After some initial studies of pure clusters, attention is now focused on the use of atoms and small molecules as probes of clusters properties.[45,46,7–9] For this purpose, one must fully understand the energetics and structural changes caused by the impurity. The change in energetics is measured by the helium chemical potential in the presence of the impurity and it is sensitive not only to the bare impurity-^{4}He interaction, but is also greatly influenced by the shell-like distribution of ^{4}He atoms near the impurity, similar to the formation of layer structure of adsorbed helium films on a plane substrate.[39,27] Obviously, the formation of such spherical layers can be similarly visualized by plotting the one-body density. The structural changes caused by impurity clearly depend on the location of the impurity.[47] Whereas unbound atomic impurities like ^{3}He, or alkali atoms, should be located at the surface, rare gas atoms and molecules that are strongly attracted to ^{4}He atoms are expected to be dissolved in the interior of the droplet. In very small clusters, such impurities will be localized at the cluster center. As the cluster grows in size, sufficient in number to completely cover the impurity and shield it from other helium atoms, the localization of the impurity, which depends on details of the many-body bound state formed between the impurity and the helium host, becomes less well defined.[47,22,7–9] In our theory, such a delocalization process is reflected dynamically in the "softening" or even instability of the cluster's collective dipole excitation.

We will consider clusters doped with a single rare gas atom or a SF_6 molecule. The stronger the impurity-^{4}He interaction, the more pronounced will be the arrangement of helium particles in spherical "shells" around the impurity. It is also possible that they exhibit shape instabilities similar to those found in adsorbed liquid films on sufficiently strongly attractive substrates.[48,27,49] Our approach is well suited to address the questions connected with the impurity energetics, localization, and the shell structure of the doped droplet. The impurity theory has been applied successfully for the case of deuterium and tritium impurities.[29] The inhomogeneous variational theory has also been applied for the study of layered structures in adsorbed films,[39,27] including the two-dimensional limit.

In all cases where a comparison with experiments or Monte Carlo data is possible, the theory provides excellent accuracy. There is therefore every reason to expect that our approach should be accurate for other impurity atoms and molecules. Additionally, we have shown in the preceding section how the excitation spectrum of our clusters is a by-product of the ground-state calculations.

A. Structure and energetics

As in Refs. 24 and 25, we neglect the zero-point motion of the impurity and treat it as a fixed, spherically symmetric, external potential added to the Hamiltonian (2.1). The interaction between the helium particles and the impurity is taken to be the Tang-Toennies potential.[50] The center-of-mass corrections derived in Appendix A are not applied. This can have quantitative consequences on some of the excitation energies, which will be discussed further below.

The energy per particle for five different impurities, Ne, Ar, Kr, Xe, and SF_6, is shown in Fig. 12. The energies for pure clusters are also shown for comparison. The introduction of impurities increases, as expected, the binding energy of the droplets in accordance to the strength of the impurity attraction. For large N, if the droplet remains stable, the energy approaches the bulk value, as it must. In the case of SF_6, the VMC and DMC calculations of Barnett and Whaley[22] are also shown for reference; note, however, that these calculations were carried out with a more recent version of the Aziz potential.[51] Our HNC/EL results have clearly a lower energy than their already substantial VMC calculation. Our results, though having the correct trend, are still systematically higher than their DMC energies. This is not unexpected since our treatment of elementary diagrams has been tested in the physically accessible range of the bulk liquid;[26] there is *a priori* no reason to expect that this treatment

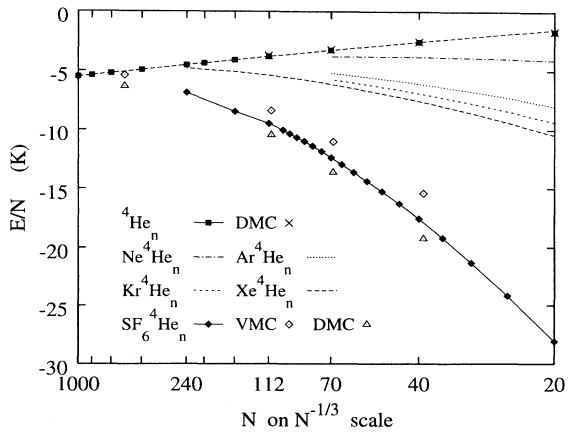

FIG. 12. The HNC/EL energies of helium clusters doped with a rare gas atom or a SF_6 impurity. Also shown are the HNC/EL energies for pure clusters, the corresponding DMC energies from Ref. 21, and the VMC energies (diamonds) and DMC energies (triangles) for SF_6-doped clusters from Ref. 22.

of elementary diagrams and triplet correlations should maintain its accuracy up to four times its intended density. The fact that it did work so well so far from its initial normalization point gives further credence to our approach.

The solvation energy of an impurity X can, in principle, be computed by calculating the energy difference,

$$\mu_N(X) \equiv E[X\ ^4\mathrm{He}_N] - E[^4\mathrm{He}_N], \tag{3.1}$$

in the limit of $N \to \infty$. However, as will be discussed in detail below, *all* doped clusters considered here are, in that limit, *unstable against the delocalization of the impurity atom.* In other words, the assumed configuration where the impurity atom remains at the center of the droplet is energetically unfavorable, and the limit $\lim_{N\to\infty} \mu_N(X)$ in principle does not exist. For the *stable* cluster sizes, the energy difference (3.1) is shown in Fig. 13 as a function of particle numbers. It is seen that all curves change relatively little for particle numbers $N > 70$. If the additional energy gained by the impurity delocalization is small, these results can still be reasonable estimates for the solvation energies. Density profiles for a sequence cluster size with a SF_6 impurity are shown in Fig. 14 and compared with available DMC results of Barnett and Whaley.[22] The profiles show the anticipated shell structure and the overall agreement with the DMC profiles is good. For the case $N = 112$ one sees the effect discussed earlier that the HNC/EL approximations produce a slightly lower saturation density, which leads to a more rapid filling of the shells. The density in the first shell of atoms is, due to the strong impurity attraction, approximately four times that of the bulk density. In the case of large droplets, one can clearly see out to the third and fourth shells. Our calculations indicate that the density of the first shell of particles around the impurity atom should increase with cluster size. This is consistent with the behavior of liquid films on plane substrates.[27] Barnett and Whaley's DMC calculations appear to show the opposite effect. The difference may well be due to the fact that Barnett and Whaley do not treat the impurity as an infinite-mass particle, but rather allow for its zero-point motion.

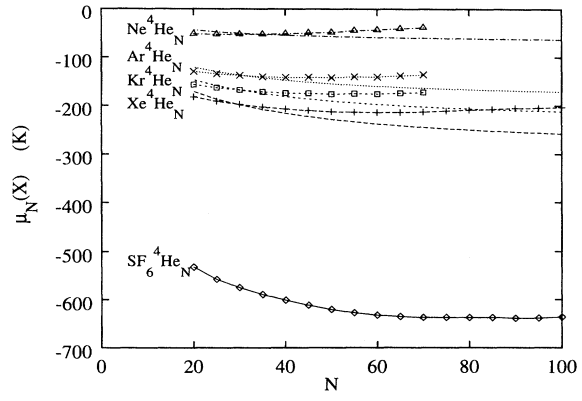

FIG. 13. The HNC/EL solvation energy (3.1) of a rare gas atom and a SF_6 impurity in helium clusters (marked lines). Also shown are the corresponding density functional calculations of Ref. 24 (unmarked lines).

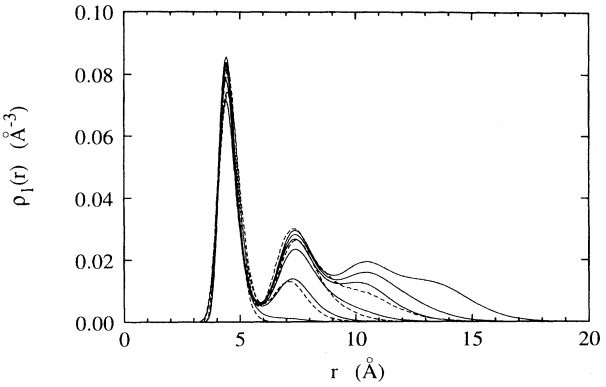

FIG. 14. Density profiles for SF_6-doped clusters. Shown are the particle numbers N =20, 40, 70, 112, 150, and 240 (solid lines) and the DMC calculations of Ref. 22 for N = 20, 39, 69, and 111 (dashed lines). Error bars on the DMC calculations are not shown for clarity.

In order to provide comparison with Dalfovo's density functional calculations, we have extracted these results from Ref. 24; the results for rare gas atoms are shown in Fig. 13. A direct comparison of Dalfovo's SF_6 solvation energy is not possible since, in order to allow for a comparison with Whaley's DMC calculation, we have used the spherically symmetric He-SF6 potential by Pack *et al.*,[52] whereas Dalfovo followed Scoles's[53] suggestion and reduced the attractive well depth. We have carried out a test calculation with a similarly less attractive potential and concluded that the energy difference of about 100 K is due to the differences between the potentials used.

A comparison between the density functional and our results shows essentially the expected behavior: For the smaller clusters, the density functional theory predicts somewhat too high energies. This is not unexpected due to the inaccuracies of density functional theory for two-dimensional systems and atomic monolayers.[28] The relevant point here is that the formation of the solvation shell of helium atoms around the impurity is essentially a two-dimensional phenomenon. However, the effect here is less severe than in helium films simply because fewer particles (12, 17, 19, 21 for Ne, Ar, Kr, and Xe, respectively, according to Ref. 24) are located in the quasi-two-dimensional solvation shell. For larger droplets, the density functional appears to overbind slightly compared to our calculation, which is a bit unexpected since the energy functional was fitted to the bulk saturation value. A more revealing comparison is that of chemical potentials, which are derivatives of the energy. This will be discussed below.

A family of density profiles of doped droplets with N=70 ^{4}He atoms is shown in Fig. 15. All of these contain basically two shells of helium atoms around the impurity. We can clearly distinguish three categories: Ne-doped droplets show the weakest shell structure, followed by Ar, Kr, and Xe which are very similar, and finally SF_6, which not only has the highest density in the first shell,

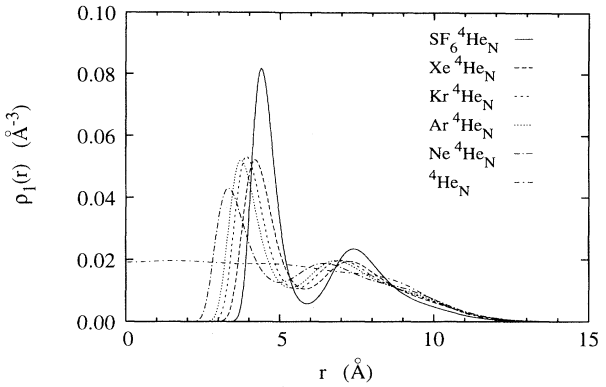

FIG. 15. The ground-state density profiles of ^{4}He droplets doped with a rare gas atom or a SF_6 impurity molecule located at the center of the droplet. Shown is the particle number $N = 70$. Also shown are the profiles for the pure droplets with $N = 70$.

but also the most pronounced minimum between the first and the second shell. It is also rather surprising that, despite differences in impurity size and range of attraction, the final doped cluster radius is virtually independent of the type of impurity.

B. Collective excitations and stability

One of the most interesting aspects of our calculations of doped clusters is the instability which favors the delocalization of the impurity atom. We have encountered this instability in an earlier and preliminary calculation on SF_6-doped droplets.[54] Here we will present a systematic study of the mass dependence of the instability and a more extended discussion. In treating the impurity as a static external field embedded in a spherically symmetric helium droplet, we cannot *directly* address the question of localization by following the motion of the impurity. However, the HNC/EL theory gives us a dynamical way of answering this question. In its unrestricted search for the energy minimum, the HNC/EL equations will not have solutions if the assumed geometric configuration is incompatible with physics dictated by the Hamiltonian. For example, if the helium atoms were not distributed spherically around the impurity (as is the case for a ^{3}He or alkali metal impurity), then the *assumed* geometry of fixing the impurity at the cluster center would not yield solutions. In other words, the HNC/EL equations have solutions only for a *relative minimum* of the energy functional within the permitted function space.

Our treatment of the impurity particle as an infinite mass object in no way compromises this special sensitivity: While the droplet can certainly not move the impurity, the helium atoms are free to move themselves away from the impurity. Such an effect would be manifested in our calculation as an instability of the *dipole excitation,* which essentially describes a relative oscillation between the impurity and the helium atoms. A dipole instability indicates that the spherically symmetric configuration with the impurity at the cluster center is *no longer* energetically favorable.

We have found, indeed, for doped clusters with sizes $N \gtrsim 50$–90, depending on the particular impurity, an instability of the dipole collective mode. Figure 16 shows the dependence of the dipole excitation energy on the cluster size and the impurity type. *All* doped clusters studied here display a dipole excitation energy that plunges through zero. The maximum stable cluster size depends essentially on the strength of the impurity-helium interaction. Weaker interacting impurities destabilize at smaller cluster sizes.

In principle, one can imagine two types of delocalization. The first is the conventional understanding that when the droplet becomes larger, the spherically symmetric droplet configuration with the impurity located at its center remains a relative energy minimum. Such an energy minimum necessarily becomes wider as the size of the droplet increases, since the surface is further away. Accompanied by this effect is an increase of the zero-point motion of either the impurity within the droplet, or, if the impurity is fixed, the droplet around the impurity. This zero-point motion corresponds to delocalization. In this scenario, the location of the center of mass of the droplet would be a broad but slightly peaked distribution about the location of the impurity. In our calculation, such a scenario would appear as a gradual convergence of the dipole excitation energy towards zero. This asymptotic value might manifest itself, due to numerical inaccuracies or approximate diagram summation, in a small positive or negative constant, but would be asymptotically, for $N \to \infty$, flat.

A second, *different* scenario occurs when the spherically symmetric configuration of the droplet as described above is no longer a *relative energy minimum.* In that case, the center of mass of the helium atoms would *not necessarily* coincide with the location of the impurity, i.e., the center of mass of the helium droplet is displaced from the impurity. Our theory is in principle able to deal with such asymmetric situations[55,56] with significant ad-

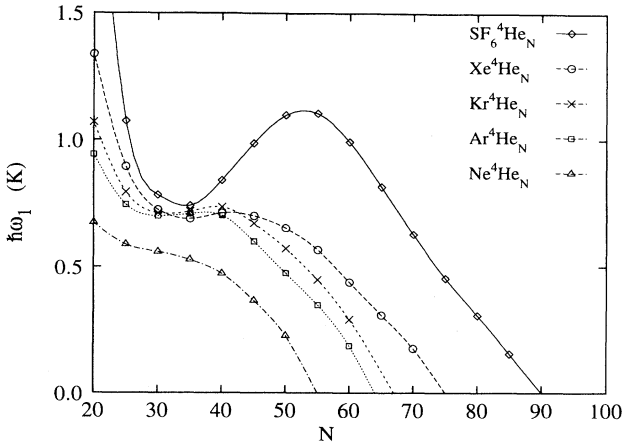

FIG. 16. The dipole excitation energies of droplets doped with a rare gas atom or a SF_6 impurity are shown as a function of particle number.

ditional effort. The present implementation addresses only the simpler question of the stability of spherically symmetric configurations with respect to infinitesimal deformations, i.e., the stability of the dipole and higher multipole modes.

Figure 16 shows no sign that these dipole energies approach an asymptotic value; in other words, our results suggest that the spherically symmetric configuration is dynamically unstable, suggesting the possibility of the second scenario.

In an approximate theory, one can never guarantee the absence of inconsistencies. In particular, in the variational/parquet-diagram theory it is known[57] that the particle-hole interaction obtained from the *second derivative of the energy with respect to the one-body density* is not identical with the particle-hole interaction appearing in the Euler equation, which stems from the *first derivative of the energy with respect to the two-body density*. Such inconsistencies normally provide useful convergence tests; we have already commented about this feature in connection with the monopole excitation above. In order to rule out that our instability is due to such an inconsistency, we have repeated the calculations for the *pure* droplets with the center-of-mass corrections turned off; in other words, we have done *exactly* the same calculation for pure droplets that was done for doped droplets. *If* the dipole instability were an artifact of the approximation, one would have expected, *in that case*, that an instability similar to the one appearing for doped droplets should occur, for even smaller particle numbers. Moreover, since the center-of-mass corrections affect *only* the dipole mode, one would also expect an unstable quadrupole mode for sufficiently large particle numbers. Quite the contrary, we observed that, for example in a pure cluster of 70 particles, the dipole mode is *raised* to approximately 0.5 K when the center-of-mass corrections are turned off. Moreover, the energetics of all multipole excitations is in very good agreement with the excitation of surface modes, as will be discussed in the next subsection.

We also note that a similar instability has been observed by Barranco and Hernandez[25] in their density functional calculation of Xe-doped droplets for the quadrupole excitation. These authors have found an instability of the *quadrupole* excitation for Xe-doped droplets on the order of 700 particles and have left blank an entry for the case of $N = 728$ in their table of quadrupole energies. Since they have not considered dipole excitations which are expected to have a lower energy, we suspect that their critical value overestimates the regime of stable clusters. Their work thus supports our view that the dipole instability is not specific to our variational theory.

Our calculation cannot proceed, without some artificial modification of the equations, beyond the cluster size where the dipole excitation energy becomes zero. It is therefore legitimate to ask how the ground-state structures and energies were obtained for clusters which are dipole unstable. Such considerations are important to ensure that this instability is not an intermittent effect that disappears for large particle numbers as one would have expected for a "shell layering effect" as described above. For cluster sizes not much greater than the "critical" size where the dipole instability occurs first, we have simply omitted the unstable dipole mode from the mode sum (A21) in the step where the static structure function needs to be computed. This can be carried out successfully for cluster sizes about 20–30 particles above the critical size. While the process is not entirely justifiable, it had little effect on other calculated quantities such as the ground-state energy, densities, or properties of the monopole. A minor consequence of this artificial stabilization is seen in the chemical potential of the Na impurity (cf. Fig. 13) which *increases* slightly for $N > 50$.

However, above the critical cluster size, continued increase in particle number eventually results in the *quadrupole* excitation also becoming unstable. To obtain solutions for even larger N, the Euler equation (2.3) was discretized and solved inside a spherical cavity that was slightly "too small" for the size of the droplet. Effectively, this shifted all excited states slightly upward to avoid the dipole instability. The necessary confinement size depends on the size of the droplet: For example, to obtain a solution for $SF_6{}^4He_{240}$ it was sufficient to confine the droplet in a box of about 20 Å radius. At this radius, the density has dropped to 10^{-5} Å^{-5}. Thus the total energy and the density profile of the cluster are essentially unaffected. However, the dipole and the quadrupole energies are increased by just enough to make the calculation feasible. Although this procedure is rather *ad hoc* with questionable physical relevance, it nevertheless yielded very reasonable energies as shown in Fig. 12. Thus ground-state energies by themselves are poor indicators of correct underlying physics.

A good illustration of the physical mechanisms of the dipole instability is provided by the excitation functions and the transition densities introduced in Appendix B. Figures 17 and 18 show the excitation functions and transition densities for two Ne and SF_6 doped droplets. One case is very stable, and the other is close to being un-

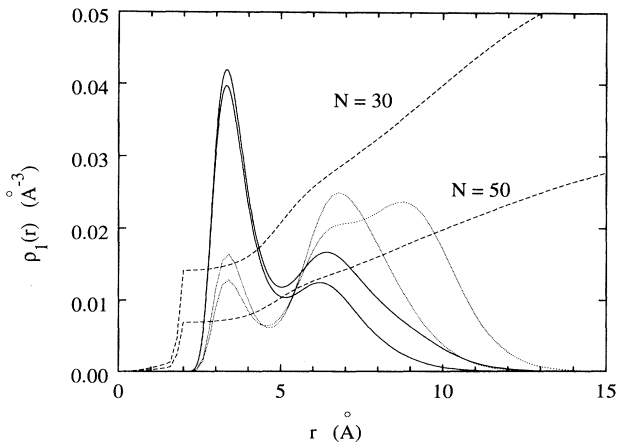

FIG. 17. The doped cluster density (solid line), the dipole excitation function (long-dashed line), and the dipole transition density (short-dashed line) are shown for two representative helium clusters doped with a Ne impurity.

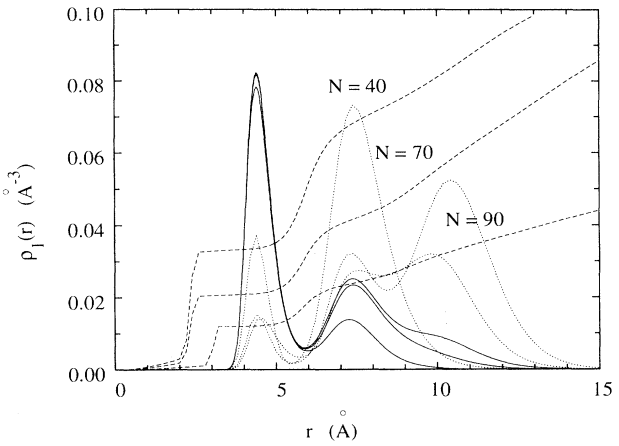

FIG. 18. The doped cluster density (solid line), the dipole excitation function (long-dashed line), and the dipole transition density (short-dashed line) are shown for three representative helium clusters doped with a SF_6 impurity.

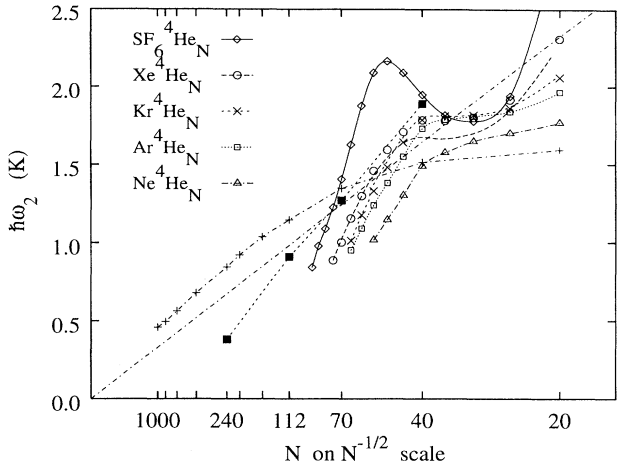

FIG. 20. Same as Fig. 19 for the quadrupole excitation energies. Also shown are the liquid drop limit (dash-dotted line) and the quadrupole excitation energies of pure clusters (dash-dotted line with crosses). The short-dashed line marked with filled squares are the quadrupole excitations calculated in density functional theory (Table III of Ref. 25).

stable. The excitation functions show basically the same picture: The first shell appears to be rigidly connected to the impurity, while particles from the second shell outward show rigid translation. As the clusters approach the critical size, the *transition densities* begin to develop a pronounced maximum near the very outer surface.

The discussion of other excitations must be viewed in light of our results for the dipole mode. Figure 19 shows the cluster size dependence of the chemical potential and the monopole excitation energy. Figure 20 shows the same dependence for the quadrupole energy. In comparison with the pure cluster case, there is an apparent lack of convergence to a "bulk limit" common to both excitations. In particular, the quadrupole excitation, which is a surface mode, should be little affected by a localized impurity at the center of the droplet. Instead, one observes in each case a clear crossover between the excitations of the doped and the pure clusters. The excitation energies of the doped clusters drop significantly below those of the pure clusters and show no sign of a bending towards the larger pure cluster values.

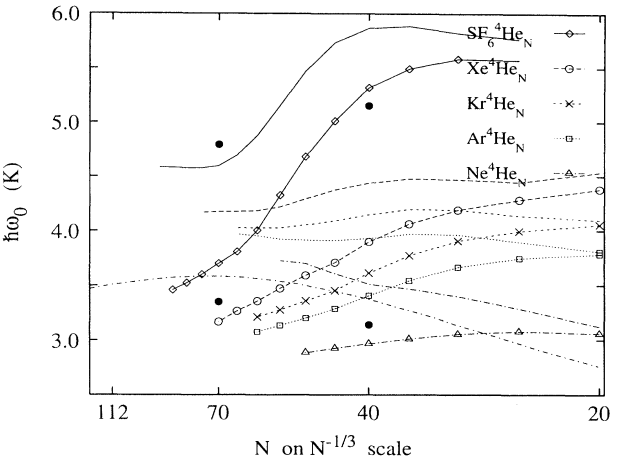

FIG. 19. The monopole excitation energies of droplets doped with SF_6 and rare gas impurities are shown as a function of particle number (marked lines). Also shown are the chemical potentials (unmarked lines) and the monopole excitation energy of the pure clusters is also shown for comparison (dash-dotted lines). The two filled circles for $N = 40$ and 70 in the lower half of the figure are chemical potentials for Xe-doped droplets from Ref. 25, and the two filled circles in the upper half of the figure are the corresponding values, for the *same* droplets, extracted from Ref. 24 as described in the text.

An interesting feature, particularly pronounced in SF_6 doped droplets, is that the chemical potential has apparently a relative minimum for particles numbers $N \sim 40$. Such a minimum would indicate that clusters of this size should be produced preferentially.

Figure 19 also shows, for the sake of comparison, chemical potentials of the ^{4}He atoms in xenon-doped clusters from the two density functional calculations, Refs. 25 and 24. The ^{4}He chemical potentials attributed to Ref. 24 were extracted from the data shown in Fig. 13 by adding our mass formula (2.10) to Eq. (3.1) and numerically differentiating. The results therefore have an uncertainty of about 0.2 K, which was estimated by trying different fits to the data. These two calculations use density functionals that differ only in details and are both fitted to reproduce the same bulk data. The resulting large discrepancy is rather inexplicable and certainly warrants further investigation.

It would, of course, be extremely interesting to see which of the features discussed above persist in the case where the impurities were allowed to move. Roughly, one would expect the monopole and the quadrupole excitation, which do not involve the motion of the center of mass, to be relatively unaffected. The dipole, on the other hand, which describes the relative motion between the impurity and the helium, should be substan-

tially modified. The effect can be estimated by scaling the excitation energy by a reduced-mass ratio. However, the point where the dipole mode becomes "soft" does not change since the excitation frequencies go to zero at this point.

IV. HIGH MULTIPOLE EXCITATIONS

One advantage of the present variational theory is the ease with which higher multipole collective excitations can be studied. Monte Carlo methods for extracting higher-ℓ partial-wave components of the two-body density become increasingly time consuming because of poor signal-to-noise ratio. This is because higher-ℓ partial-wave components require weighting with higher-order Legendre polynomials, whose rapid oscillations produce very weak signals for Monte Carlo binning. As a part of the optimization process, we have computed all *discrete* excitation energy for all angular momenta $\ell \geq 2$. Since the excitation function is generally given by $\sim r^\ell$, these high-ℓ excitations are essentially surface vibrational modes. In general, one expects the droplet excitation energies to depend on both N, the droplet size, and ℓ, the multipolarity or angular symmetry. However, if a surface mode ℓ were to be excited by a projectile with momentum $\hbar k$, then by conservation of angular momentum, k must be on the order of

$$k = \sqrt{\ell(\ell+1)}/R, \tag{4.1}$$

where we can take the droplet radius to be the equivalent hard-sphere radius $R = \sqrt{5/3}r_{\rm rms}$. This then suggests that, instead of viewing the excitation energies as separately depending on both ℓ and N, one should plot them in terms of a single variable, k. The validity of this picture is dramatically demonstrated in Fig. 21. The excitation energies for all droplets, ranging from $N = 20$ to 1000, nearly fall on a universal curve. The only two noticeable deviations are the lowest $\ell = 2$, 3 excitation energies of cluster size $N = 20$. This is a classic case of scaling behavior, where the *a priori* joint dependence of ℓ and N collapses down to just k. Moreover, the surface excitation energies are in excellent agreement with the *experimentally observed* surface excitations of helium films.[58] It is perhaps to be expected that the surface excitations of a spherical droplet must be qualitatively similar to that of a film or a plane surface; what is surprising is the extent of the quantitative agreement even for cluster sizes of only about 100 atoms. This good agreement in turn allows us to infer and check on the droplet excitations by use of experimental film data. At small $k < 0.30$, the spectrum can be well fitted by a characteristic "ripplon" dispersion relation,

$$\hbar\omega = 12.399\,k^{3/2} + 0.043 \ \text{K}. \tag{4.2}$$

Comparing this fit with the familiar ripplon dispersion relation,

$$\omega^2(k) = \frac{\sigma}{m\rho_\infty}k^3, \tag{4.3}$$

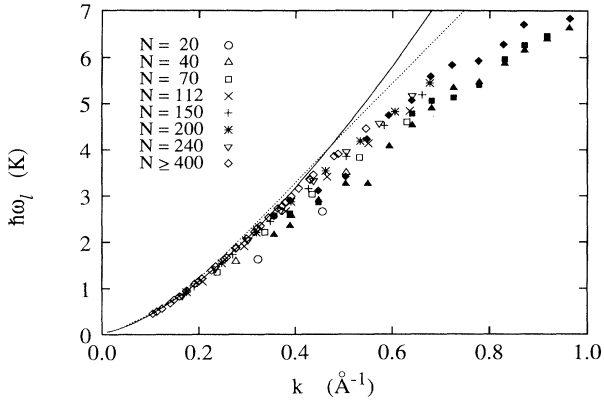

FIG. 21. The lowest excitation energies with an angular momentum up to $\ell = 9$ are shown, for all pure ^{4}He droplets considered here, as a function of an effective wave number $k = \sqrt{\ell(\ell+1)}/R$, where we have taken $R \equiv \sqrt{5/3}r_{\rm rms}$. The droplets with $N \geq 150$ are marked with diamonds, $N = 112$ with asterisks, $N = 70$ with crosses, $N = 40$ with triangles, and $N = 20$ with squares. Only energies corresponding to discrete modes are shown. Also shown is the lowest excitation energy of a *helium film* adsorbed to a graphite substrate (dashed line, from Ref. 34). The figure is from Ref. 66.

allows us to extract from the dispersion relation a surface energy of $\sigma = 0.279$ K Å^{-2}, in excellent agreement with the one obtained from our mass formula (2.10). This clearly demonstrates the consistency of our theoretical descriptions of both the ground and excited states. Since ours is a variational calculation, it is not too surprising that the entire fit is shifted upward by an amount 0.043 K. The smallness of this constant shift also gives us some sense of the systematic error involved. Since the calculation is *a priori* not an upper bound, we are particularly gratified for this indication that it is. The fitted curve (4.2) is plotted as a solid line in Fig. 21. Both the droplet excitations and the ripplon dispersion relation Eq. (4.2) also agree very well with that of a film of liquid helium atoms adsorbed onto a *plane* substrate.[33,34] The Feynman spectrum for a film of three layers' thickness is shown in Fig. 21 as the upper dashed line. The accuracy of the Feynman approximation can be assessed by allowing for time-dependent *pair-correlation functions* in the trial function (2.21); this generalization produces significant improvements of the excitation spectrum in the vicinity of the roton minimum,[59,60] but produces no significant change of the ripplon dispersion relation within the "bandwidth" of the universal curve.

At shorter wavelengths, the excitation spectrum of the surface mode in helium has been measured in neutron scattering experiments.[58] Data from these measurements are shown as solid markers in Fig. 21. The considerable overlap between theoretical droplet energies and experimental film data suggests that the latter can be inverted to yield information on the excitations of even very small droplets with $\approx$ 100 atoms. This experimental connection is highly significant in view of the fact that very little is known experimentally about the energetics of pure helium droplets.

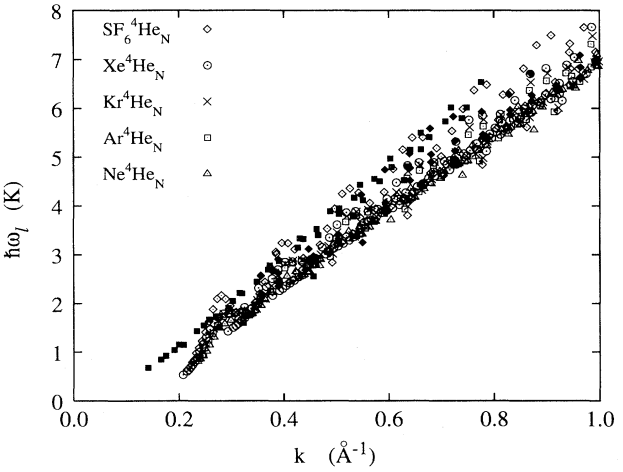

FIG. 22. The lowest discrete excitation energies are shown, for all pure and doped helium droplets considered here, as a function of an effective wave number $k = \sqrt{\ell(\ell+1)}/R$, where we have taken $R \equiv \sqrt{5/3}r_{\rm rms}$. Doped droplets are marked by open symbols as indicated in the figure, pure droplets are shown as solid squares, and experimental data of the lowest excitation energy of a *helium film* adsorbed to a graphite substrate are shown as solid diamonds.

The apparent universality of the surface-mode dispersion relation persists for the case of doped clusters. Figure 22 compares the discrete, high angular momentum modes of *all* doped clusters investigated here with those of pure clusters and the experimental ripplon dispersion relation of liquid films. We find a band that follows essentially the surface-phonon dispersion relation of pure droplets, and has a sharp lower boundary. Typically, *smaller* droplet excitations are found at the upper edge of the band, and larger droplet excitations at the lower edge. This lower edge is systematically *below* the dispersion relation of pure droplets. This is consistent with our above result that the droplets become unstable by a softening of the outermost shell of particles around the impurity.

V. DYNAMIC STRUCTURE FUNCTION

Up to now, we have focused on the low-lying, discrete, collective excitations which have revealed much about the microscopic structure and stability of helium droplets. However, as described previously,[61,21,28,34] our theory is also capable of computing high-lying resonances in the continuum, as in the case of the dynamic structure function. In our present theory of the excitation, the dynamic structure function $S(k,\omega)$ can be obtained directly from the Fourier transform of the transition densities (2.24),

$$S(k,\omega) = |\delta\tilde{\rho}_\omega(\mathbf{k})|^2, \tag{5.1}$$

with

$$\delta\tilde{\rho}_\omega(\mathbf{k}) = \int d^3k e^{i\mathbf{k}\cdot\mathbf{r}}\delta\rho(\mathbf{r}). \tag{5.2}$$

Normally, one obtains $S(k,\omega)$ in a partial-wave expansion,

$$S(k,\omega) = \sum_\ell S_\ell(k,\omega), \tag{5.3}$$

and both the individual components and the total sum are of interest. In Ref. 21 only the lowest three modes were considered. We have also demonstrated there that the excitation of low angular momentum modes contributes relatively little to the total scattering cross section of a plane wave; it is therefore necessary to include partial waves of high multipolarity. We have seen already above that our calculation of the low-lying *discrete* excitations with higher multipole symmetry led to very reasonable results; we now also must include the high-lying continuum states.

In general, one would expect for large droplets a picture similar to the two-mode picture seen in adsorbed films, namely, a phonon-roton mode reminiscent of the bulk dispersion relation, and a surface mode. However, neither the size dependence nor the relative strength of these modes is known. Observing these two modes, for example, by neutron or x-ray scattering experiments, would have significant advantages over experiments on adsorbed films, since structures like the two-dimensional phonon would not be present. Moreover, contrasting film and droplet excitation spectra could provide a clean separation of the relevant physics.

Figures 23–25 show the dynamic structure function

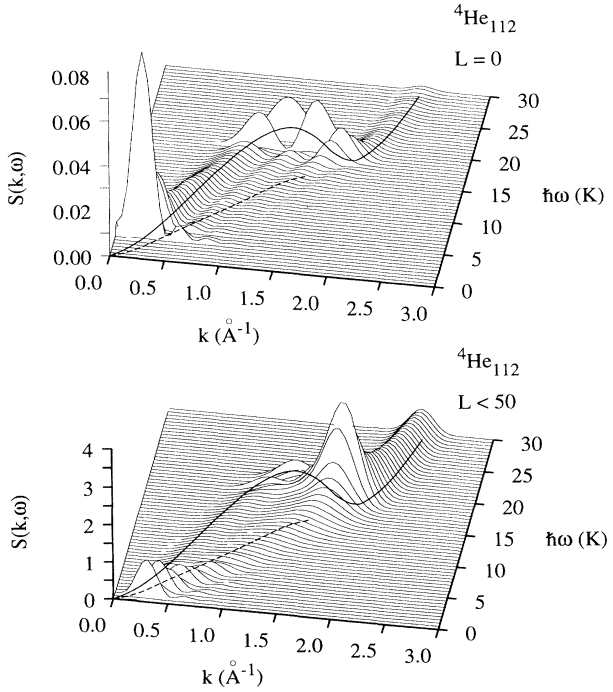

FIG. 23. Dynamic structure function of a helium droplet with $N = 112$ for the $\ell = 0$ component only (upper figure) and the full structure function (lower figure). Note that the scales are not the same. The solid curve in the $k - \hbar\omega$ plane of the figure is the Feynman phonon-roton spectrum for the bulk liquid, and the dashed curve the surface excitation calculated in Ref. 34; see also Fig. 21.

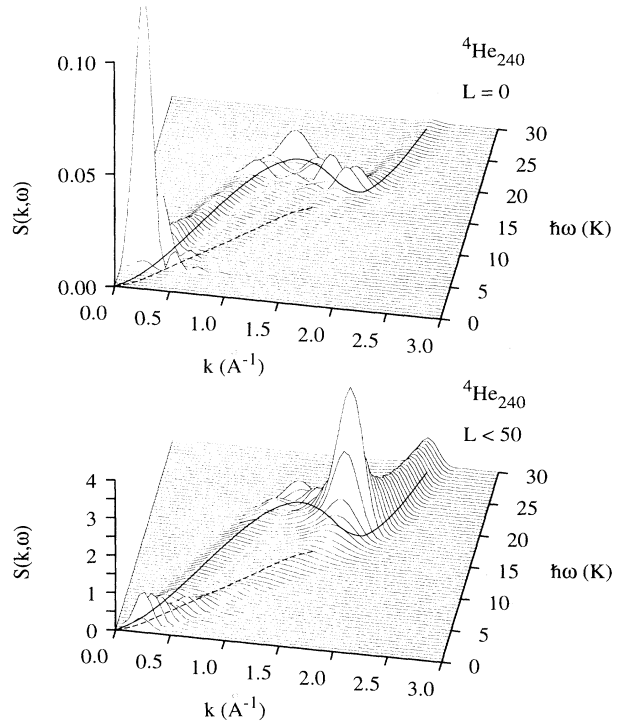

FIG. 24. Same as Fig. 23 for $N = 240$

for a medium size and two of the larger droplets considered here. In order to display the discrete excitation modes discussed in the previous sections, we have broadened these modes by a Gaussian of 0.5 K width. In all cases, we show both the monopole component and the full dynamic structure function, which is summed over the first 50 angular momentum components. In the monopole component, we see of course at low energies the breathing (monopole) mode discussed earlier. Both cases $N = 112$ and $N = 240$ display a number of remarkably well-defined resonances for energies in the area between the maxon and the roton minimum. These resonances have disappeared for $N = 1000$. In all three cases, we see strength along a narrow band in the energy-momentum plane that follows precisely the bulk phonon/maxon/roton curve. Small clusters also display some parallel "diffractive echoes" of the first main ridge of the phonon branch at higher momenta. These echoes reflect finite-size effects and have mostly disappeared for $N = 1000$.

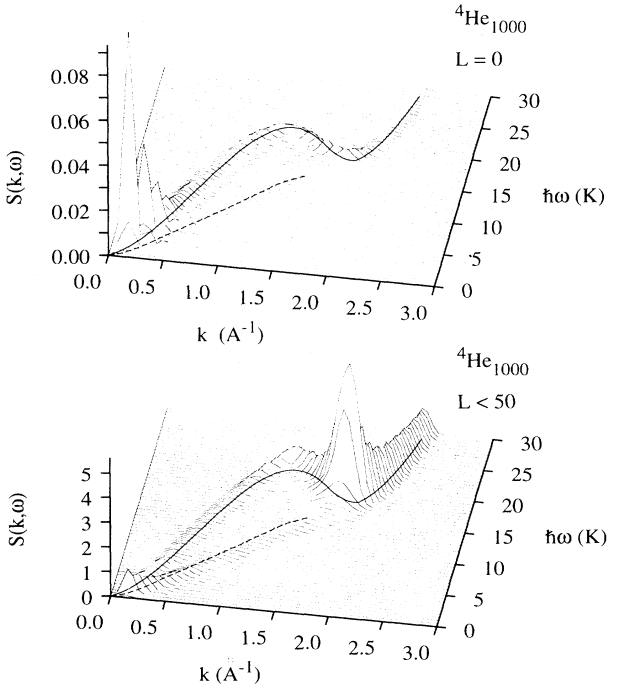

FIG. 25. Same as Fig. 23 for $N = 1000$.

The picture changes radically for the full structure function, when *all* relevant angular momentum components are included in the expansion (5.3). We found that approximately 50 angular momentum components were sufficient for the sum to converge; cf. Fig. 9. Note that while the *absolute* scale of the $S(k,\omega)$ is arbitrary, the *relative* scale between all figures is significant. Obviously, the full $S(k,\omega)$ is about a factor of 50 larger than its monopole component. For the full dynamic structure function, a clear second resonance branch appears, which follows the dispersion relation of the *surface excitations* discussed earlier in Sec. IV.

For $N = 112$, this "ripplon branch" is quite broad and poorly defined, but it dominates significantly in strength over the bulklike, but relatively weak, phonon-roton branch. In all cases, the finite size of the system is reflected in a number of still quite visible discrete resonances at low energies. As the particle number is increased, both resonance branches become narrower; the phonon-roton gains and the ripplon loses relative strength. Most significantly, in all cases, the strength at the location of the roton minimum is significantly increased. (Note that the increase in strength here is like a curved "wall," still faithfully following the bulk Feynman curve.) Even more interesting and important is that, for N =1000, up to a wave vector is approximately 1.5 Å^{-1}; the phonon and the ripplon branch have comparable strength. This suggests an intriguing possibility to observe both excitations in a situation that is not contaminated by substrate effects.

In particular, we saw *no* evidence for a "roton minimum" in these surface excitations of droplets. This provides further evidence for the interpretation[33,34] that the roton minimum observed in liquid helium films[62,58] is *not* a "surface roton," but rather an excitation within the bulk liquid or one of the highly compressed liquid layers of these adsorbed films. Of course, this observation does not preclude the existence of a "roton minimum" in the general (nonsurface continuum) excitation spectrum of clusters. In fact, as we shall see in the next section, *both* the phonon-roton spectrum and the surface ripplon spectrum can be simultaneously made manifest in the dynamic structure function.

Figure 25 appears to suggest a "hybridization" between the phonon and the ripplon at wave numbers close to the location of the roton minimum, and we hasten to point out that such an interpretation is *not* correct.

The strength of the surface mode comes from excitations with *high* angular momentum, given essentially by Eq. (4.1) with $k_{\rm eff} \approx 2$, leading to $\ell \sim 40$. The phonon-roton branch, on the other hand, originates essentially from low angular momentum contributions $\ell < 20$. The agreement of the energies of these two modes at the roton minimum is accidental. The comparison with liquid films is again useful. There, the collective excitations have been calculated[34] in an approximation that allows for time-dependent pair correlations in the Feynman function (2.21). By this generalization, the energy of the roton minimum is lowered by almost a factor of 2, whereas the corrections to the surface mode are more moderate and essentially on the relative scale shown in Fig. 21. In other words, the degeneracy between the surface and the volume mode is an artifact of the Feynman approximation.

The dynamic structure function of *doped* droplets is profoundly different. As an extreme case, we show in Fig. 26 the $\ell = 0$ component and the full $S(k,\omega)$ of a droplet with $N = 112$ and an SF_6 impurity. While the low-energy breathing mode has comparable strength to the one found in pure droplets, *all* the monopole resonances around the maxon/roton region have disappeared. When all angular momenta are taken into account, some resonances appear in that energy/momentum regime, but the strength is fragmented and displaced. Up to k =1.5 Å^{-1}, no significant strength is found along the bulk phonon branch, whereas the resonance along the ripplon curve is very similar to the pure case. This result is consistent with our previous finding in Sec. IV that the surface excitations are only weakly affected by the presence of the impurity. In this case, the resonances may have appeared at slightly higher energies due to the "squeezing" needed to stabilize the droplet as described in Sec. III B. The strong influence of the presence of the impurity, which essentially alters and to some extent "freezes" the short-range structure of the droplets, on the strength of the excitations in the vicinity of the roton minimum is plausible, since the wavelength of the excitations is of the length scale comparable to the local structure induced by the impurity.

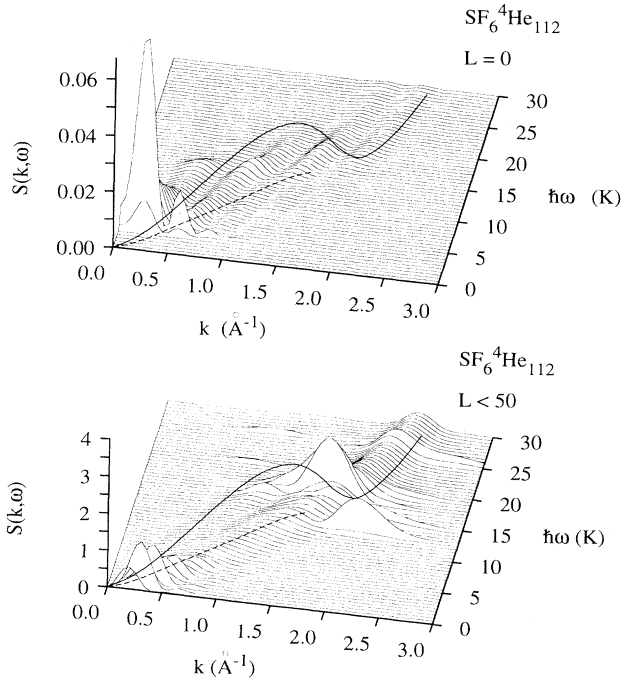

FIG. 26. Same as Fig. 25 for a SF_6-doped droplet with $N = 112$.

VI. SUMMARY AND CONCLUSIONS

Both pure and doped helium clusters are unique bosonic systems of great intrinsic interest. Because of the relatively simple ^{4}He-^{4}He interaction, they are also excellent laboratories for testing our theoretical understanding of finite quantum many-body systems. In this paper, we have demonstrated that the use of the variational HNC/EL theory can yield results that are beyond what has been calculable via Monte Carlo methods in terms of cluster size, high angular momentum excitations, and total dynamic structure functions. This in turn has allowed us to bridge the gap between finite systems and the bulk limit, for example, in seeing how the bulk Feynman spectrum emerges out of the cluster dynamic structure function. On the theoretical side, we have (1) obtained excellent ground-state energies for pure droplets via HNC/EL which extrapolated correctly to the bulk value with a very reasonable surface energy; (2) confirmed the existence of density oscillations in helium droplets heretofore much disputed in Monte Carlo calculations; (3) further validated the HNC/EL approach by showing excellent results for the pair-distance and pair-correlation distribution functions; (4) computed the high angular momentum collective bound states, and demonstrated that the excitation energies scale in the effective wave number variable k, and that the ripplon dispersion relation is obeyed at small k with about the right surface energy; (5) showed that for a finite droplet, the full dynamic structure function simultaneously displays both the phonon-roton and the ripplon excitation spectrum; and (6) yielded very good ground-state energies for doped droplets and revealed the instability of the dipole mode.

Some of these findings have direct experimental implications; in particular, we may emphasize the following.

(a) The low-energy, high angular momentum excitation energies of pure clusters not only scale in the variable k essentially independent of the size of the cluster, they are also in excellent agreement with the experimentally observed spectrum for surface excitations. Thus one can invert the experimental data to yield information on the excitation energies of these elusive pure helium droplets.

(b) Our result that *all* doped systems exhibit an instability against the delocalization of the impurity atom is intriguing and clearly warrants further investigation. This instability is also implicit in some recent density functional calculations,[25] where the quadrupole modes of doped clusters were found not to converge to their bulk limit. We have since performed VMC calculations[35]

which clearly show that SF_6 at least delocalizes in the conventional manner, i.e., the center-of-mass distribution of the droplet becomes increasingly broad with droplet size, but remains slightly peaked about the impurity. More exact DMC calculations attempting to verify the second scenario by directly computing the droplets' center-of-mass distribution have so far, due to the latter's slow convergence and strong trial function dependence, remained inconclusive and controversial.[35,36] Our result that the maximum stable cluster size should decrease with weaker impurity attraction may serve as a guide for selecting desirable doped clusters for future investigations. In any case, our study of the dipole instability has reopened the discussion on the localization of impurities in helium droplets. Whereas prior to our work, it seems to have been generally accepted that the SF_6 should be fairly rigidly localized at the droplet center, now attention is shifted to understand the precise scenario and the extent of delocalization. Such theoretical efforts are just in time to confront growing experimental data[7,8] on the infrared absorption spectrum of SF_6 in helium clusters. In particular, deciding the extent of SF_6 delocalization in helium droplets will help to understand whether or not the splitting of the spectrum will have a simple explanation, such as the SF_6 molecule is located near the surface.

(c) In computing the full dynamic structure function by summing up to $\ell = 50$ modes, we found that even for a $N = 1000$ droplet, the surface and the volume excitation are still of comparable strength. Thus if the dynamic structure function of a "fog" of helium droplets could be measured, this would provide a cleaner laboratory than adsorbed films to detect surface excitations. This could also provide important feedback for the analysis of neutron scattering experiments in helium films. As the droplets become smaller, we have shown how the relative *overall* strength of the phonon/roton branch was reduced.

Note added in proof. (a) We have since carried out extensive diffusion Monte Carlo calculations on the SF_6 impurity with much improved importance sampling functions (Ref. 35). The resulting DMC density profiles beyond the first peak are in very good agreement with HNC/EL results, much better than is shown on Fig. 14 when compared to an earlier DMC calculation (Ref. 22). Recent DMC calculations[36] using our improved trial function or longer running time are also in much better agreement with HNC/EL results. (b) In further discussions with S. Hernandez and M. Barranco, we have learned that their chemical potentials for xenon-doped droplets of Ref. 25 (as shown in Fig. 19) are unlikely to be correct.

ACKNOWLEDGMENTS

This work was supported, in part, by the National Science Foundation Grant Nos. PHY92-13502 (to S.A.C.), PHY91-08066 and INT90-14040 (to E.K.), and PHY89-04035 to the Institute for Theoretical Physics (ITP) in Santa Barbara. E.K. thanks the ITP for the warm hospitality and support during the spring of 1994. Our paper profited from discussions with R. Barnett, M. Barranco, C. E. Campbell, D. Ceperley, W. Kohn, M. Saarela, and B. Whaley. We thank R. Barnett, M. Barranco, D. Ceperley, F. Dalfovo, M. Saarela, S. Stringari, and B. Whaley for communication of unpublished material. The computations have been carried out on an IBM RS/6000-590 which was provided by IBM for benchmarking purposes. We would like to thank IBM for providing us with this opportunity.

APPENDIX A: CENTER-OF-MASS MOTION AND THE EULER EQUATION

For the manipulations that follow, we ignore triplet correlations since these do not lead to any further insight. Using the usual Jackson-Feenberg integration by parts, one obtains for the center-of-mass energy (2.8)

$$T_{\rm cm} = -\frac{\hbar^2}{2M}\sum_i \frac{\langle\Psi_0 \mid \nabla_i^2 \mid \Psi_0\rangle}{\langle\Psi_0 \mid \Psi_0\rangle} - \frac{\hbar^2}{2M}\sum_{i\neq j}\frac{\langle\Psi_0 \mid \nabla_i\cdot\nabla_j \mid \Psi_0\rangle}{\langle\Psi_0 \mid \Psi_0\rangle}$$
$$= -\frac{\hbar^2}{4M}\sum_i \frac{\langle\Psi_0 \mid [\nabla_i^2 U] \mid \Psi_0\rangle}{\langle\Psi_0 \mid \Psi_0\rangle} - \frac{\hbar^2}{4M}\sum_{i\neq j}\frac{\langle\Psi_0 \mid [\nabla_i\cdot\nabla_j U] \mid \Psi_0\rangle}{\langle\Psi_0 \mid \Psi_0\rangle}, \tag{A1}$$

where

$$U = \sum_i u_1(\mathbf{r}_i) + \sum_{i<j} u_2(\mathbf{r}_i,\mathbf{r}_j). \tag{A2}$$

The first term in Eq. (A1) is structurally identical to the kinetic energy expression for nonuniform geometries; it causes a reduction of the ordinary Jackson-Feenberg energy expression by a factor $1-m/M$. Only pair (and possibly triplet) correlations contribute to the second term, which can be written as

$$-\frac{\hbar^2}{4M}\sum_{i\neq j}\langle\Psi_0 \mid [\nabla_i\cdot\nabla_j U] \mid \Psi_0\rangle$$
$$= -\frac{\hbar^2}{4M}\int d^3r_1 d^3r_2 \rho_2(\mathbf{r}_1,\mathbf{r}_2)\nabla_1\cdot\nabla_2 u_2(\mathbf{r}_2,\mathbf{r}_2). \tag{A3}$$

The Born-Green-Yvon equation is employed, as usual, to eliminate the one-body correlations $u_1(\mathbf{r})$, which leads to the total energy expression

$$E_{\rm int} = \frac{\hbar^2}{2m^*}\int d^3r \left|\nabla\sqrt{\rho(\mathbf{r})}\right|^2 + \frac{1}{2}\int d^3r_1 d^3r_2 \rho_2(\mathbf{r}_1,\mathbf{r}_2) V_{\rm JF}(\mathbf{r}_1,\mathbf{r}_2)$$
$$\equiv T + E_c, \tag{A4}$$

where

$$V_{\rm JF}(\mathbf{r}_1,\mathbf{r}_2) = v(|\mathbf{r}_1-\mathbf{r}_2|) - \frac{\hbar^2}{8m^*}\left\{[D(1)+D(2)]\,u_2(\mathbf{r}_1,\mathbf{r}_2) - 2\frac{m^*}{M}\nabla_1\cdot\nabla_2 u_2(\mathbf{r}_1,\mathbf{r}_2)\right\} \tag{A5}$$

is a center-of-mass corrected version of the Jackson-Feenberg effective potential. Here, $1/m^* = 1/m - 1/M$, and $D(i) = \rho^{-1}(\mathbf{r}_i)\nabla \cdot [\rho(\mathbf{r}_i)\nabla]$. Thus, the only modifications induced by the subtraction of the center-of-mass energy are a reduced mass and the term $\nabla_1 \cdot \nabla_2 u_2(\mathbf{r}_1, \mathbf{r}_2)$.

The Euler equation is conveniently derived using the prime-equation technique:[63,38]

$$\frac{\hbar^2}{8m^*}\left[D(1) + D(2) - 2\frac{m^*}{M}\nabla_1 \cdot \nabla_2\right]\rho_2(\mathbf{r}_1, \mathbf{r}_2) = \rho_2'(\mathbf{r}_1, \mathbf{r}_2), \quad \text{(A6)}$$

where

$$\rho_2'(\mathbf{r}_1, \mathbf{r}_2) = \int d^3r_3 d^3r_4 \frac{\delta\rho_2(\mathbf{r}_3, \mathbf{r}_3)}{\delta u_2(\mathbf{r}_1, \mathbf{r}_1)} V_{\mathrm{JF}}(\mathbf{r}_1, \mathbf{r}_2) \quad \text{(A7)}$$

is formally defined the same way as in the case of an infinite system.[38] The remaining operations are identical to the ones carried out in the nonuniform, infinite system and do not need to be repeated here. The essential steps are to use the HNC equation to eliminate the pair-correlation function $u_2(\mathbf{r}_1, \mathbf{r}_2)$ in favor of the pair-distribution function $g(\mathbf{r}_1, \mathbf{r}_2)$, and to reformulate the Euler equation in terms of a "particle-hole interaction" $V_{\text{p-h}}(\mathbf{r}_1, \mathbf{r}_2)$ and the "direct correlation function" $X(\mathbf{r}_1, \mathbf{r}_2)$. Useful abbreviations are the "tilde" notation,

$$\tilde{A}(\mathbf{r}_1, \mathbf{r}_2) \equiv \sqrt{\rho(\mathbf{r}_1)}A(\mathbf{r}_1, \mathbf{r}_2)\sqrt{\rho(\mathbf{r}_2)} \quad \text{(A8)}$$

and the convolution product,

$$[A * B](\mathbf{r}_1, \mathbf{r}_2) \equiv \int d^3r_3 A(\mathbf{r}_1, \mathbf{r}_3)B(\mathbf{r}_3, \mathbf{r}_2). \quad \text{(A9)}$$

The static structure function $S(\mathbf{r}_1, \mathbf{r}_2)$ [Eq. (2.6)] is related to the direct correlation function $\tilde{X}(\mathbf{r}_1, \mathbf{r}_2)$ through

$$S(\mathbf{r}_1, \mathbf{r}_2) = \left[\mathbf{1} - \tilde{X}(\mathbf{r}_1, \mathbf{r}_2)\right]^{-1}, \quad \text{(A10)}$$

where both the unit operator and the inverse in Eq. (A10) are to be understood in the sense of the convolution product (A9). Further useful quantities are a local one-body Hamiltonian,

$$H_1^*(\mathbf{r}) = -\frac{\hbar^2}{2m^*}\frac{1}{\sqrt{\rho_1(\mathbf{r})}}\nabla\rho_1(\mathbf{r}) \cdot \nabla\frac{1}{\sqrt{\rho_1(\mathbf{r})}}, \quad \text{(A11)}$$

and a center-of-mass correction term

$$\delta H_1(\mathbf{r}_1, \mathbf{r}_2) \equiv -\frac{\hbar^2}{2M}\frac{\nabla_1 \cdot \nabla_2\rho_2(\mathbf{r}_1, \mathbf{r}_2)}{\sqrt{\rho_1(\mathbf{r}_1)\rho_1(\mathbf{r}_2)}}, \quad \text{(A12)}$$

such that a total "one-body Hamiltonian" has the form

$$H_1(\mathbf{r}_1, \mathbf{r}_2) = H_1^*\delta(\mathbf{r}_1 - \mathbf{r}_2) + \delta H_1(\mathbf{r}_1, \mathbf{r}_2). \quad \text{(A13)}$$

The "one-body Hamiltonian" (A13) is the same as the one derived in the translationally invariant Feynman theory of collective excitations;[21] it also plays a central role in the optimized HNC theory. In terms of the quantities introduced above, the Euler equation can be cast, after some algebraic manipulations, into the form

$$\left[S^{-1} * H_1 * S^{-1}\right](\mathbf{r}_1, \mathbf{r}_2) = H_1^* + 2\tilde{V}_{\text{p-h}}(\mathbf{r}_1, \mathbf{r}_2), \quad \text{(A14)}$$

where

$$V_{\text{p-h}}(\mathbf{r}_1, \mathbf{r}_2) = g(\mathbf{r}_1, \mathbf{r}_2)v(r_{12}) + t(\mathbf{r}_1, \mathbf{r}_2) + h(\mathbf{r}_1, \mathbf{r}_2)w_I(\mathbf{r}_1, \mathbf{r}_2) + \frac{\hbar^2}{4M}\nabla_1 \cdot \nabla_2 X(\mathbf{r}_1, \mathbf{r}_2), \quad \text{(A15)}$$

with the kinetic energy

$$t(\mathbf{r}_1, \mathbf{r}_2) = \frac{\hbar^2}{2m}\left[\left|\nabla_1\sqrt{g(\mathbf{r}_1, \mathbf{r}_2)}\right|^2 + \left|\nabla_2\sqrt{g(\mathbf{r}_1, \mathbf{r}_2)}\right|^2\right] - \frac{\hbar^2}{2M}\left|(\nabla_1 + \nabla_2)\sqrt{g(\mathbf{r}_1, \mathbf{r}_2)}\right|^2 \quad \text{(A16)}$$

and the induced potential

$$\tilde{w}_I(\mathbf{r}_1, \mathbf{r}_2) = -\tilde{V}_{\text{p-h}}(\mathbf{r}_1, \mathbf{r}_2) - \frac{1}{2}\left[H_1^* * \tilde{h} + \tilde{h} * H_1^*\right](\mathbf{r}_1, \mathbf{r}_2) - \frac{\hbar^2}{4M}\frac{\nabla_1 \cdot \nabla_2\rho_2(\mathbf{r}_1, \mathbf{r}_2)}{\sqrt{\rho_1(\mathbf{r}_1)\rho_1(\mathbf{r}_2)}} - \frac{\hbar^2}{4M}\sqrt{\rho_1(\mathbf{r}_1)\rho_1(\mathbf{r}_2)}\nabla_1 \cdot \nabla_2 N(\mathbf{r}_1, \mathbf{r}_2). \quad \text{(A17)}$$

The above generalization of the HNC/EL equations to a system with center-of-mass motion is algebraically somewhat unpleasant, but should be tractable if necessary. For our purposes it is important, however, to keep in mind that for almost all features the center-of-mass motion is a negligible effect, and normally produces corrections to the equations that are smaller than the anticipated accuracy. Before we turn to a numerical application of the theory, we therefore study the Euler equation in order to determine those features of the center-of-mass motion that are essential to keep.

The Euler equation (A14) is most conveniently discussed and solved by normal-mode decomposition.[38] In the present case, one solves the eigenvalue problem,

$$\left[H_1^* + 2\tilde{V}_{\text{p-h}}\right] * H_1\psi_\omega = \hbar^2\omega^2\psi_\omega. \quad \text{(A18)}$$

Adopting the normalization

$$(\psi_\omega \mid H_1 \mid \psi_{\omega'}) = \hbar\omega\delta_{\omega\omega'} \quad \text{(A19)}$$

and defining

$$\phi_\omega(\mathbf{r}) = \frac{1}{\hbar\omega}H_1\psi_\omega(\mathbf{r}), \quad \text{(A20)}$$

one can represent the static structure function as

$$S(\mathbf{r}_1, \mathbf{r}_2) = \sum_\omega \phi_\omega(\mathbf{r}_1)\phi_\omega(\mathbf{r}_2) \quad \text{(A21)}$$

and its inverse as

$$S^{-1}(\mathbf{r}_1, \mathbf{r}_2) = \sum_\omega \psi_\omega(\mathbf{r}_1)\psi_\omega(\mathbf{r}_2). \quad \text{(A22)}$$

The summation in Eqs. (A21) and (A22) is to be understood as an integration when the spectrum is continuous.

An immediate consequence of the normal-mode decomposition (A21) is that the eigenfunctions also satisfy the relation

$$[H_1 * \psi_\omega](\mathbf{r}) = \hbar\omega\,[S * \psi_\omega](\mathbf{r}), \tag{A23}$$

which is identical to the Feynman relation derived in Ref. 21. This relation also shows that the eigenfunctions $\psi_\omega(\mathbf{r})$ are related to the Feynman excitation functions, and that the $\phi_\omega(\mathbf{r})$ are related to the transition density; cf. Eq. (B1).

APPENDIX B: PROPERTIES OF THE EULER EQUATION

In order to discuss the mathematical properties and physical interpretation of the Euler equation, we first show that the particle-hole interaction as defined above can indeed be identified with the second variational derivative of the internal energy with respect to the one-body density. The same precautions apply as in the infinite system: we need to carry out the variation *for fixed pair-correlation functions* $u_2(\mathbf{r}_1,\mathbf{r}_2)$, and not assume any approximation like HNC. Keeping $u_2(\mathbf{r}_1,\mathbf{r}_2)$ fixed, and varying $u_1(\mathbf{r})$, we obtain

$$\begin{aligned}\delta\rho_1(\mathbf{r}_1) &= \rho_1(\mathbf{r}_1)\delta u_1(\mathbf{r}_1) + \int d^3r_2\,[\rho_2(\mathbf{r}_1,\mathbf{r}_2) - \rho_1(\mathbf{r}_1)\rho_1(\mathbf{r}_2)]\,\delta u_1(\mathbf{r}_2)\\ &= \sqrt{\rho_1(\mathbf{r}_1)}\int d^3r_2 S(\mathbf{r}_1,\mathbf{r}_2)\sqrt{\rho_1(\mathbf{r}_2)}\delta u_1(\mathbf{r}_2).\end{aligned} \tag{B1}$$

To calculate the second variation of the energy, we first carry out the variation with respect to $u_1(\mathbf{r})$, assuming that the pair-correlation function has been optimized. One obtains the familiar Feynman expression,

$$\begin{aligned}\delta^2_{u_1}E_{\rm int} &= \frac{1}{2}\frac{\langle\Psi_0 \mid [\delta u_1\,[T - T_{\rm cm}, \delta u_1]] \mid \Psi_0\rangle}{\langle\Psi_0 \mid \Psi_0\rangle}\\ &= \frac{1}{\langle\Psi_0 \mid \Psi_0\rangle}\left\langle\Psi_0\left|\frac{\hbar^2}{2m}\sum_i|\nabla_i\delta u_1(\mathbf{r}_i)|^2 - \frac{\hbar^2}{2M}\left|\sum_i\nabla_i\delta u_1(\mathbf{r}_i)\right|^2\right|\Psi_0\right\rangle\\ &= \frac{\hbar^2}{2m^*}\int d^3r\rho_1(\mathbf{r})\,|\nabla\delta u_1(\mathbf{r})|^2 - \frac{\hbar^2}{2M}\int d^3r_1d^3r_2\rho_2(\mathbf{r}_1,\mathbf{r}_2)\nabla\delta u_1(\mathbf{r}_1)\cdot\nabla\delta u_1(\mathbf{r}_2)\\ &= \int d^3r_1d^3r_2\sqrt{\rho_1(\mathbf{r}_1)}\delta u_1(\mathbf{r}_1)H_1(\mathbf{r}_1,\mathbf{r}_2)\delta u_1(\mathbf{r}_2)\sqrt{\rho_1(\mathbf{r}_2)}.\end{aligned} \tag{B2}$$

Using Eq. (B1) and the Euler equation (A14) now indeed shows that

$$\frac{\delta^2E_{\rm int}}{\delta\rho_1(\mathbf{r}_1)\delta\rho_1(\mathbf{r}_2)} = V_{\text{p-h}}(\mathbf{r}_1,\mathbf{r}_2) \text{ for } \mathbf{r}_1 \neq \mathbf{r}_2. \tag{B3}$$

An important property of the one-body Hamiltonian is that it has *two* zero-energy eigenfunctions. These are the monopole solution $\psi_{0,0}(r) = \sqrt{\rho_1(r)}$ which corresponds to a renormalization of the wave function, and the dipole solution $\psi_{0,1}(\mathbf{r}) = \mathbf{c}\cdot\mathbf{r}\sqrt{\rho_1(r)}$, where $\mathbf{c}$ is a fixed vector. Only the second statement requires proof:

$$\begin{aligned}H_1\psi_{0,1}(\mathbf{r}) &= -\frac{\hbar^2}{2m^*}\frac{1}{\sqrt{\rho_1(r)}}\nabla\cdot\mathbf{c}\rho_1(r) + \frac{\hbar^2}{2M}\int d^3r'\frac{\nabla\cdot\mathbf{c}\rho_2(\mathbf{r},\mathbf{r}')}{\sqrt{\rho_1(\mathbf{r})}}\\ &= -\frac{\hbar^2}{2m^*}\frac{\mathbf{c}\cdot\nabla\rho_1(r)}{\sqrt{\rho_1(r)}} + \frac{\hbar^2}{2M}\frac{\mathbf{c}\cdot\nabla}{\sqrt{\rho_1(r)}}\int d^3r'\rho_2(\mathbf{r},\mathbf{r}')\\ &= -\frac{\hbar^2}{2m^*}\frac{\mathbf{c}\cdot\nabla\rho_1(r)}{\sqrt{\rho_1(r)}} + \frac{\hbar^2(N-1)}{2M}\frac{\mathbf{c}\cdot\nabla\rho_1(r)}{\sqrt{\rho_1(r)}} = 0\end{aligned} \tag{B4}$$

where the sequential relation

$$\int d^3r'\,[\rho_2(\mathbf{r},\mathbf{r}') - \rho_1(\mathbf{r})\rho_1(\mathbf{r}')] = -\rho_1(\mathbf{r}) \tag{B5}$$

was used. The excitation function $\phi_{0,1}(\mathbf{r}) = \mathbf{c}\cdot\mathbf{r}\sqrt{\rho_1(r)}$ corresponds to a rigid translation of the droplet.[21]

It is also interesting to see how the invariance of the internal energy under rigid translation appears as a zero-energy eigenfunction of the *adjoint* Euler equation,

$$H_1 * \left[H_1^* + 2\tilde{V}_{\text{p-h}}\right]\phi_\omega = \hbar^2\omega^2\phi_\omega. \tag{B6}$$

Note that $\sqrt{\rho_1(\mathbf{r})}\phi_\omega(\mathbf{r}) = \delta\rho_1(\mathbf{r})$. An infinitesimal rigid translation $\rho_1(\mathbf{r}) \to \rho_1(\mathbf{c}+\mathbf{r})$ would correspond to a density change $\delta\rho_1(\mathbf{r}) = \mathbf{c}\cdot\nabla\rho_1(\mathbf{r})$; in other words, $\phi_0(\mathbf{r}) = \mathbf{c}\cdot\nabla\sqrt{\rho(\mathbf{r})}$ should be a zero-energy eigenfunction of Eq. (B6).

To see that, recall that the one-body density is calculated by minimizing the internal energy $E_{\rm int}$ with respect

to the density, which leads to a Hartree equation,

$$\left[-\frac{\hbar^2}{2m^*}\nabla^2 + V_H(\mathbf{r})\right]\sqrt{\rho(\mathbf{r})} = \mu\sqrt{\rho(\mathbf{r})}, \tag{B7}$$

where μ is the chemical potential, and

$$V_H(\mathbf{r}) \equiv \frac{\delta E_{\rm int}}{\delta\rho_1(\mathbf{r})} \tag{B8}$$

is a generalized Hartree potential.

An important identity in this geometry follows, in a manner similar to the free surface[64,65] by considering a rigid displacement of the density as above. The Hartree potential $V_H(\mathbf{r})$ must move with the density, i.e.,

$$V_H[\rho_1(\mathbf{r}+\mathbf{c})](\mathbf{r}) = V_H[\rho_1(\mathbf{r})](\mathbf{r}+\mathbf{c}). \tag{B9}$$

Expanding the Hartree potential to first order in $\mathbf{c}$, we obtain

$$\begin{aligned} V_H(\mathbf{r}+\mathbf{c}) &= V_H(\mathbf{r}) + \mathbf{c}\cdot\nabla V_H(\mathbf{r}) \\ &= V_H(\mathbf{r}) + \int d^3r' V_{\text{p-h}}(\mathbf{r},\mathbf{r}')\mathbf{c}\cdot\nabla\rho_1(\mathbf{r}'), \end{aligned} \tag{B10}$$

i.e.,

$$\nabla V_H(\mathbf{r}) = \int d^3r' V_{\text{p-h}}(\mathbf{r},\mathbf{r}')\nabla\rho_1(\mathbf{r}'). \tag{B11}$$

From Eq. (B11) and the Hartree equation (B7) it follows that $\nabla\sqrt{\rho_1(\mathbf{r})}$ is a zero-energy eigenfunction of the operator $H_1^* + 2\tilde{V}_{\text{p-h}}$, i.e.,

$$H_1^*\nabla\sqrt{\rho_1(\mathbf{r})} + 2\int d^3r'\tilde{V}_{\text{p-h}}(\mathbf{r},\mathbf{r}')\nabla\sqrt{\rho_1(\mathbf{r})} = 0. \tag{B12}$$

The relationship is easily verified by calculating the gradient of the Hartree equation (B7) and using the property (B11).

There is an important difference between the identity (B12) and the zero-energy properties of the operator H_1 discussed above. The properties of H_1 depend only on the sequential relation (B5); they are therefore satisfied with numerical accuracy if the pair density is computed by optimization. The property (B12) depends, on the other hand, on the feature (B3), which is normally satisfied only in an exact theory. On the other hand, violating the property (B12) may lead to spurious "excitations" and possibly instabilities of the variational problem.

For practical calculations, it is necessary to include only those consequences of the center-of-mass motion which lead to the specific features of the Euler equation discussed above. The eigenvalue problem (A18) can be decoupled and solved by expanding the excitation function and the two-body density in partial waves,

$$\psi_\omega(\mathbf{r}) \equiv \psi_{\omega,\ell}(r)Y_{\ell,m}(\hat{\mathbf{r}}), \tag{B13}$$

and, for example,

$$\tilde{V}_{\text{p-h}}(\mathbf{r},\mathbf{r}') = \sum_\ell \frac{2l+1}{4\pi}V_\ell(r,r')P_\ell(\hat{\mathbf{r}}\cdot\hat{\mathbf{r}}'). \tag{B14}$$

In this representation, the zero-energy modes appear only in the monopole and the dipole channels. Since generally center-of-mass corrections are expected to be smaller than the anticipated accuracy of our calculation, in particular for the larger droplets, we have therefore included the center-of-mass term δH_1 [Eq. (A12)] only for $\ell = 1$. To guarantee that any inconsistency between the particle-hole interaction and the Hartree potential does not cause spurious excitation energies, we have, for the pure clusters, projected the operator $H_1^* + 2\tilde{V}_{\text{p-h}}$ into a subspace orthogonal to the zero-energy eigenfunction $\nabla\sqrt{\rho_1(\mathbf{r})}$. In passing, we note however, that the matrix element of the (unprojected) operator with the function $\nabla\sqrt{\rho_1(\mathbf{r})}$ is very small (typically 10^{-1} K) compared with all of its eigenvalues in the orthogonal subspace.

APPENDIX C: TRIPLET CORRELATIONS

The general theory of optimized triplet correlations has been described in Ref. 27; it is sufficient here to concentrate on the specifics of the spherical geometry. The formulation of the three-body correction given there has been turned towards the normal-mode analysis formulated in Appendix A. Adopting the partial-wave decomposition (B13), the full $S(\mathbf{r}_1,\mathbf{r}_2)$ is represented as a bilinear combination of angular momentum and energy eigenfunctions,

$$S(\mathbf{r}_1,\mathbf{r}_2) = \sum_{n,\ell,m}\phi_{n,\ell}(r_1)\phi_{n,\ell}(r_2)Y_{\ell,m}(\hat{\mathbf{r}}_1)Y^*_{\ell,m}(\hat{\mathbf{r}}_2). \tag{C1}$$

The key ingredient of the theory is a triplet matrix element V_{abc}, where each of the state labels a, b, c, is a triple of quantum numbers $\{\omega_a,\ell_a,m_a\}$. Adopting the working formulas of Ref. 27 [Eq. (A.29)], the triplet vertex is

$$\begin{aligned} V_{abc} &= -\frac{\hbar^2}{2m}\int d^3r_1 d^3r_2 d^3r_3\sqrt{\rho(r_1)}\sqrt{\rho(r_2)}\sqrt{\rho(r_3)}\phi_a(\mathbf{r}_1)\phi_b(\mathbf{r}_2)\phi_c(\mathbf{r}_3) \\ &\quad\times[\nabla_1 X(\mathbf{r}_1,\mathbf{r}_2)\cdot\nabla_1 X(\mathbf{r}_1,\mathbf{r}_3) + \text{cycl.}] \\ &= -V_{\omega_a\ell_a\omega_b\ell_b\omega_c\ell_c}\int d\Omega Y_{\ell_a,m_a}(\hat{\mathbf{r}})Y_{\ell_b,m_b}(\hat{\mathbf{r}})Y_{\ell_c,m_c}(\hat{\mathbf{r}}), \end{aligned} \tag{C2}$$

with

$$V_{\omega_a \ell_a \omega_b \ell_b \omega_c \ell_c} = \int dr \xi_{\omega_a \ell_a}(r) \Big[\zeta'_{\omega_b \ell_b}(r) \zeta'_{\omega_c \ell_c}(r) - \frac{1}{2r^2} \left[\ell_a(\ell_a+1) - \ell_b(\ell_b+1) - \ell_c(\ell_c+1) \right] \zeta_{\omega_b \ell_b}(r) \zeta_{\omega_c \ell_c}(r) \Big] + \text{cycl.}, \tag{C3}$$

where, as in the surface case,

$$\zeta_{\omega_b \ell_b}(r) = \frac{\psi_{\omega_b \ell_b}(r) - \phi_{\omega_b \ell_b}(r)}{r\sqrt{\rho(r)}} \tag{C4}$$

and

$$\xi_{\omega_b \ell_b}(r) = r\sqrt{\rho(r)} \phi_{\omega_b \ell_b}(r). \tag{C5}$$

Inserting this into the triplet energy gives

$$\begin{aligned} E_3 &= -\frac{1}{24} \sum_{abc} \frac{|V_{abc}|^2}{\hbar(\omega_a + \omega_b + \omega_c)} \\ &= -\frac{1}{24} \sum_{\omega_a \ldots \ell_c} \frac{|V_{\omega_a \ell_a \omega_b \ell_b \omega_c \ell_c}|^2}{\hbar(\omega_a + \omega_b + \omega_c)} \sum_{m_a m_b m_c} \left| \int d\Omega Y_{\ell_a, m_a}(\hat{\mathbf{r}}) Y_{\ell_b, m_b}(\hat{\mathbf{r}}) Y_{\ell_c, m_c}(\hat{\mathbf{r}}) \right|^2 \\ &= -\frac{(4\pi)^2}{24} \sum_{\omega_a \ldots \ell_c} \frac{|V_{\omega_a \ell_a \omega_b \ell_b \omega_c \ell_c}|^2}{\hbar(\omega_a + \omega_b + \omega_c)} \frac{(2\ell_a+1)(2\ell_b+1)(2\ell_c+1)}{(4\pi)^3} \begin{pmatrix} a & b & c \\ 0 & 0 & 0 \end{pmatrix}^2 . \end{aligned} \tag{C6}$$

[1] S. Gspann, in *Physics of Electronic and Atomic Collisions*, edited by S. Datz (North-Holland, Amsterdam, 1982), p. 79.
[2] P. W. Stephens and J. G. King, Phys. Rev. Lett. **51**, 1538 (1983).
[3] E. Syskakis, F. Pobell, and H. Ullmaier, Phys. Rev. Lett. **55**, 2964 (1985).
[4] H. Buchenau *et al.*, J. Chem. Phys. **91**, 6875 (1990).
[5] J. Gspann, Phys. Status Solidi B **169**, 519 (1991).
[6] T. Jiang and J. A. Northby, Phys. Rev. Lett. **68**, 2620 (1992).
[7] S. Goyal, D. L. Schutt, and G. Scoles, Phys. Rev. Lett. **69**, 933 (1992).
[8] S. Goyal, D. L. Schutt, and G. Scoles, J. Phys. Chem. **97**, 2236 (1993).
[9] R. Fröchtenicht, J. P. Toennies, and A. Viselov, Chem. Phys. Lett. **229**, 1 (1994).
[10] U. Helmbrecht and J. G. Zabolitzky, in *Monte Carlo Methods in Quantum Problems*, edited by M. Kalos (D. Reidel, Holland, 1984).
[11] V. R. Pandharipande *et al.*, Phys. Rev. Lett. **50**, 1676 (1983).
[12] V. R. Pandharipande, S. C. Pieper, and R. B. Wiringa, Phys. Rev. B **34**, 4571 (1986).
[13] P. Sindzingre, M. J. Klein, and D. M. Ceperley, Phys. Rev. Lett. **63**, 1601 (1989).
[14] M. Casas and S. Stringari, J. Low Temp. Phys. **79**, 135 (1990).
[15] M. V. R. Krishna and K. B. Whaley, Phys. Rev. Lett. **64**, 1126 (1990).
[16] M. V. R. Krishna and K. B. Whaley, J. Chem. Phys. **93**, 6738 (1990).
[17] S. A. Chin and E. Krotscheck, Phys. Rev. Lett. **65**, 2658 (1990).
[18] J. W. Halley, C. E. Campbell, C. F. Giese, and K. Goetz, Phys. Rev. Lett. **71**, 2429 (1993).
[19] C. E. Campbell, J. Low Temp. Phys. **93**, 907 (1993).
[20] S. A. Chin, J. Low Temp. Phys. **93**, 921 (1993).
[21] S. A. Chin and E. Krotscheck, Phys. Rev. B **45**, 852 (1992).
[22] R. N. Barnett and K. B. Whaley, J. Chem. Phys. **99**, 9730 (1993).
[23] S. Stringari and J. Treiner, J. Chem. Phys. **87**, 5021 (1987).
[24] F. Dalfovo, Z. Phys. D **29**, 61 (1994).
[25] M. Barranco and E. S. Hernandez, Phys. Rev. B **49**, 12 078 (1994).
[26] E. Krotscheck and M. Saarela, Phys. Rep. **232**, 1 (1993).
[27] B. E. Clements, J. L. Epstein, E. Krotscheck, and M. Saarela, Phys. Rev. B **48**, 7450 (1993).
[28] B. E. Clements, H. Forbert, E. Krotscheck, and M. Saarela, J. Low Temp. Phys. **95**, 849 (1994).
[29] M. Saarela and E. Krotscheck, J. Low Temp. Phys. **90**, 415 (1993).
[30] E. Krotscheck (unpublished).
[31] N. Pavloff and J. Treiner, J. Low Temp. Phys. **83**, 331 (1991).
[32] B. E. Clements *et al.*, J. Low Temp. Phys. **89**, 585 (1992).
[33] B. E. Clements *et al.*, in *XX International Conference on Low Temperature Physics*, edited by R. J. Donelly (North-Holland, Amsterdam, 1994), Vols. 194–196, pp. 659, 660.
[34] B. E. Clements *et al.*, Phys. Rev. B **50**, 6958 (1994).
[35] S. A. Chin and E. Krotscheck, in *Recent Progress in Many Body Theories*, edited by E. Schachinger, H. Mitter, and H. Sorrmann (Plenum, New York, 1995), Vol. 5.
[36] M. A. McMahon, R. N. Barnett, and K. B. Whaley (un-

published).
[37] R. A. Aziz *et al.*, J. Chem. Phys. **70**, 4330 (1979).
[38] E. Krotscheck, Q.-X. Qian, and W. Kohn, Phys. Rev. B **31**, 4245 (1985).
[39] E. Krotscheck, Phys. Rev. B **32**, 5713 (1985).
[40] M. Iino, M. Suzuki, and A. J. Ikhushima, J. Low Temp. Phys. **61**, 155 (1985).
[41] R. de Bruyn Ouboter and C. N. Yang, Phys. B+C **144B**, 127 (1986).
[42] F. Dalfovo, A. Lastri, and S. Stringari (unpublished).
[43] R. Schiavilla *et al.*, Nucl. Phys. A **473**, 267 (1987).
[44] C. C. Chang and M. Cohen, Phys. Rev. B **11**, 1059 (1975).
[45] A. Scheidemann, B. Schilling, J. P. Toennies, and J. A. Northby, Phys. Status Solidi B **165/166**, 135 (1990).
[46] A. Scheidemann, J. P. Toennies, and J. A. Northby, Phys. Rev. Lett. **64**, 1899 (1990).
[47] X. J. Gu *et al.*, J. Chem. Phys. **93**, 4898 (1990).
[48] B. E. Clements, E. Krotscheck, and H. J. Lauter, Phys. Rev. Lett. **70**, 1287 (1993).
[49] M. Wagner and D. Ceperley, J. Low Temp. Phys. **94**, 185 (1994).
[50] K. T. Tang and J. P. Toennies, Z. Phys. D **1**, 91 (1986).
[51] R. A. Aziz, F. R. W. McCourt, and C. C. K. Wong, Mol. Phys. **61**, 1487 (1987).
[52] R. T. Pack, E. Piper, G. A. Pfeffer, and J. P. Toennies, J. Chem. Phys. **80**, 4940 (1984).
[53] G. Scoles, Int. J. Quantum Chem. **24**, 475 (1990).
[54] E. Krotscheck and S. A. Chin, Chem. Phys. Lett. **227**, 143 (1994).
[55] E. Krotscheck, M. Saarela, and J. L. Epstein, Phys. Rev. Lett. **61**, 1728 (1988).
[56] B. E. Clements, E. Krotscheck, and M. Saarela, J. Low Temp. Phys. (to be published).
[57] A. D. Jackson, A. Lande, and R. A. Smith, Phys. Rev. Lett. **54**, 1469 (1985).
[58] H. J. Lauter, H. Godfrin, V. L. P. Frank, and P. Leiderer, Phys. Rev. Lett. **68**, 2484 (1992).
[59] C. C. Chang and C. E. Campbell, Phys. Rev. B **13**, 3779 (1976).
[60] J. Suominen and M. Saarela, in *Condensed Matter Theories*, edited by J. Keller (Plenum, New York, 1989), Vol. 4, p. 377.
[61] E. Krotscheck and C. J. Tymczak, Phys. Rev. B **45**, 217 (1992).
[62] H. J. Lauter, H. Godfrin, V. L. P. Frank, and P. Leiderer, in *Excitations in Two-Dimensional and Three-Dimensional Quantum Fluids*, Vol. 257 of *NATO Advanced Study Institute, Series B: Physics*, edited by A. F. G. Wyatt and H. J. Lauter (Plenum, New York, 1991), p. 419.
[63] E. Feenberg, *Theory of Quantum Liquids* (Academic, New York, 1969).
[64] G. Bertsch, Phys. Rev. A **9**, 819 (1974).
[65] B. E. Clements, E. Krotscheck, and M. Saarela, Z. Phys. B **94**, 115 (1994).
[66] S. A. Chin and E. Krotscheck, Phys. Rev. Lett. **74**, 1143 (1995).